

Chapter 4

Robust Closed-Loop Control of the Bouncing Ball

If the facts don't fit the theory,
change the facts.

Albert Einstein

4.1 Introduction

As illustrated in Chapter 3, open-loop stabilization of the bouncing ball requires negative acceleration of the actuator at impact (eq. (3.19), see Schaal et al., 1996). In contrast, the mirror law algorithms have been designed in closed-loop and can consequently afford positive acceleration at impact. The aim of this chapter is to discuss the role of acceleration tuning for *robust* closed-loop design of the bouncing ball dynamics with *limited* feedback, i.e. when the complete ball trajectory cannot be sensed as in the mirror law implementation. We focus on the measurement of the *impact times* as sole discrete output. This information provides a source of “rhythmic” feedback, directly available through auditive or haptic inflows for human subjects. Such a design is also cheap and efficient in robotics, since the times of impact can be measured by cheap sensors, like accelerometers (recording the vibrations on the actuator), microphones, etc. . .

In human juggling experiments, it has long been recognized that the control of timing is ubiquitous, either for throwing and catching time in the three-balls cascade (Amazeen et al., 1999) or for 1D ball bouncing (see Section 3.4 and Sternad et al., 2001b). This has been further emphasized recently in a robotic experiment by Hirai and Miyazaki (2006). They studied a juggling-like ball-passing task in the horizontal plane (i.e. no effect of gravity) whose stabilization is based only on feedback measurement of the impact times between the balls and the robot. The objective of the present chapter is to emphasize the role of impact times as a central information

for the *model-based* feedback control of the bouncing ball and to demonstrate the existence of *robust* control schemes based on this sole discrete information. The measurement of the occurrences of timed events, like the impacts in this task, could obviously be generalized as an exclusive source of feedback for most rhythmic systems. For example, in locomotion, the initiation and/or termination of the stance phase are marked periodic events in the cycle that could be useful for feedback.

The 1D bouncing ball dynamics (Holmes, 1982; Guckenheimer and Holmes, 1986) have been reviewed in Section 3.2 of this thesis. The actuation is the continuous-time motion $s(t)$. The ball dynamics are governed by the gravitational field g and the impacts with the actuator. The complete bouncing ball dynamics are described by the discrete *Poincaré map* (3.4) (flight map) and (3.5) (impact rule), whose state is the impact position $s[k]$ and post-velocity $v[k]$. Given a reference trajectory $(s_\rho[\bullet], v_\rho[\bullet])$ for the system (3.4), (3.5), we study the design of a *continuous-time* motion $s(t)$ that achieves asymptotic tracking of this *discrete* reference.

We first derive a controller that achieves deadbeat tracking of an *arbitrary* reference trajectory (Sections 4.2.3 and 4.2.4). This controller is a *state* feedback controller, which is then turned into an *output* feedback controller (Section 4.2.5): the state of the ball is reconstructed from the sole impact times by means of a deadbeat observer. The output feedback controller assigns the impact position and the impact velocity of the actuator but the stability of the closed-loop system puts no constraints on the impact *acceleration*. In contrast, this parameter turns to be a crucial design parameter in the *robustness* analysis of the closed-loop system (Section 4.3). We focus the robustness analysis on the model uncertainty arising from the impact model. The design is based on the simple Newton's impact model and we model the uncertainty by treating the variations of the coefficient of restitution as an external disturbance. By a proper tuning of the acceleration at impact, simulation results illustrate that the uncertainty on the coefficient of restitution can be efficiently rejected.

4.2 Feedback Control of the Bouncing Ball

4.2.1 The sinusoidal actuation vs. the mirror law

In Chapter 3, we introduced two actuation laws to stabilize the period-one motion of the bouncing ball. First, the sinusoidal actuation (3.7) is purely open-loop and stabilizes the period-one motion if the amplitude and frequency are tuned according to (3.17) (Holmes, 1982; Guckenheimer and Holmes, 1986; Bapat et al., 1986). The stability of the orbit implies that the actuator acceleration at impact is *negative* (Schaal et al., 1996) in the range given by (3.19). This is illustrated in Fig. 4.1, top.

In contrast with the sensorless sinusoidal law, the *mirror law* is a feedback strategy based upon permanent tracking of the ball (Buehler, Koditschek and Kindlmann, 1988, 1990, 1994). Its simplest version has been derived in Section 3.3. In steady-state, the mirror law behavior is reproduced in Fig. 4.1, bottom.

The two control strategies that stabilize the same pattern are clearly distinct in term of feedback requirement. The first one is sensorless while the second requires a permanent tracking of the ball. Comparing the sinusoidal law and the mirror law in Fig. 4.1, we see that both of them stabilize the bouncing ball period-one at the same steady-state (s^*, v^*) , but with significant differences in the underlying continuous-time control law. We observe that the sinusoidal trajectory is decelerating at impact while the mirror law is accelerating. It suggests that the acceleration at impact possibly influences the feedback requirements of the control law.

4.2.2 Stabilization with sensorless sinusoidal actuation

Even if there is no control loop with the sensorless sinusoidal actuation $s(t) = A \sin(\omega t)$, it is of interest to interpret its stabilizing feedback mechanism in the system dynamics.

The linearized state-space equations (3.14) and (3.15) can be written under the following matrix form:

$$\begin{aligned} \begin{pmatrix} \frac{\omega}{g} \delta v[k+1] \\ \omega \delta t[k+1] \end{pmatrix} &= \begin{pmatrix} e^2 & 0 \\ 1 & 1+e \end{pmatrix} \begin{pmatrix} \frac{\omega}{g} \delta v[k] \\ \omega \delta t[k] \end{pmatrix} \\ &\quad + \begin{pmatrix} -(1+e) \frac{A\omega^2}{g} \sqrt{1 - \left(\frac{(1-e)\pi n g}{(1+e)A\omega^2} \right)^2} \\ 0 \end{pmatrix} \omega \delta t[k+1] \\ &= \left(\underbrace{\begin{pmatrix} e^2 & 0 \\ 1 & 1+e \end{pmatrix}}_{\tilde{\mathbf{A}}_{BB}} + \underbrace{\begin{pmatrix} -(1+e) \frac{A\omega^2}{g} \sqrt{1 - \left(\frac{(1-e)\pi n g}{(1+e)A\omega^2} \right)^2} \\ 0 \end{pmatrix}}_{\tilde{\mathbf{B}}_{BB}} \right) \underbrace{\begin{pmatrix} 1 & 1+e \end{pmatrix}}_{\tilde{\mathbf{C}}_{BB}} \begin{pmatrix} \frac{\omega}{g} \delta v[k] \\ \omega \delta t[k] \end{pmatrix} \end{aligned} \quad (4.1)$$

which is obviously equivalent to (3.16), with $\mathbf{A}_{BB} = \tilde{\mathbf{A}}_{BB} + \tilde{\mathbf{B}}_{BB} \tilde{\mathbf{C}}_{BB}$.

Eq. (4.1) admits the following state-space representation:

$$\mathbf{x}[k+1] = \tilde{\mathbf{A}}_{BB} \mathbf{x}[k] + \tilde{\mathbf{B}}_{BB}(A, \omega) u[k] \quad (4.2)$$

$$\begin{aligned} y[k] &= t[k+1] \\ &= \tilde{\mathbf{C}}_{BB} \mathbf{x}[k] \end{aligned} \quad (4.3)$$

where the ‘‘controller input’’ equals the ‘‘output’’: $u[k] = y[k]$, i.e. the impact time $t[k+1]$. This state-space representation is both controllable and observable.

In this representation, the sinusoidal actuation is interpreted as a proportional feedback of the output $t[k+1]$, emphasizing the importance of estimating the *next impact time* for stabilization. The first element of the matrix $\tilde{\mathbf{B}}_{BB}$ is a feedback gain equal to the actuator acceleration at impact. Negative feedback thus requires a negative acceleration.

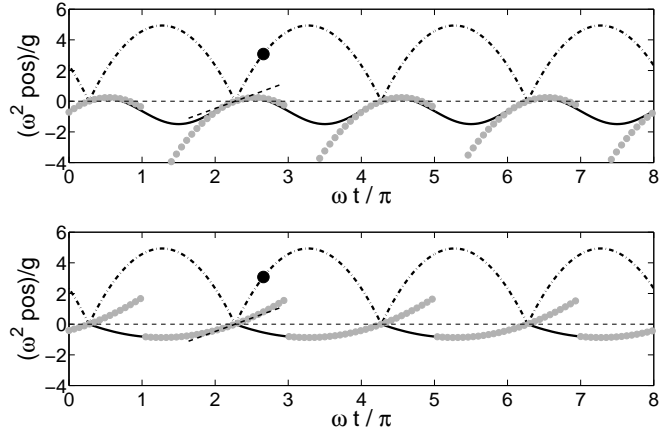


Figure 4.1: Comparison of the sinusoidal trajectory (top) and the mirror law (bottom) to stabilize the period-one pattern. The actuator (respectively the ball) non-dimensional position is depicted with solid (respectively dash-dotted) lines over non-dimensional time. The gray dots denote the piecewise quadratic trajectory that match the actuator position, velocity and acceleration at impact, see Section 4.2.3.

4.2.3 State feedback control

This section describes a more general class of controllers aiming at tracking a *time-varying* referenced trajectory, impact after impact. Given the flight time equation (3.6), exact matching between the real and the referenced next impact position, i.e.

$$s[k+1] = s_\rho[k+1] \quad (4.4)$$

is provided if the next impact occurs at time

$$t_u[k+1] = t[k] + \frac{v[k] + \sqrt{v[k]^2 - 2g(s_\rho[k+1] - s[k])}}{g}. \quad (4.5)$$

Given (3.5) and (4.5), the impactor velocity at impact must be equal to

$$\dot{s}_u[k+1] = \frac{v_\rho[k+1] - e\sqrt{v[k]^2 - 2g(s_\rho[k+1] - s[k])}}{1+e} \quad (4.6)$$

in order to provide $v[k+1] = v_\rho[k+1]$.

As illustrated in Fig. 4.1, the two control laws described in Section 4.2.1 achieve the same stabilization objective, but differ in the impact acceleration. In order to illustrate how the actuator acceleration at impact influences the robustness of the feedback system, we consider at first a mathematically convenient family of control laws in the form of a piecewise quadratic function of time, re-initialized after each impact:

$$s(t) = s_u[k+1] + \dot{s}_u[k+1](t - t_u[k+1]) + \frac{\gamma}{2}(t - t_u[k+1])^2 \quad (4.7)$$

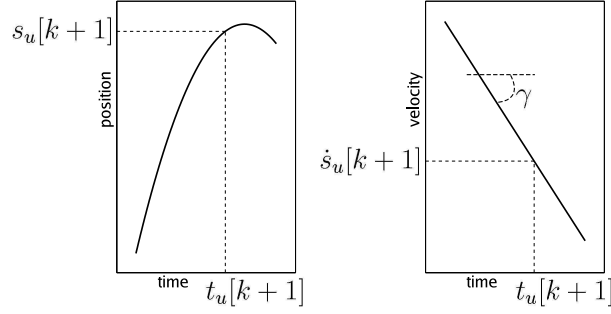


Figure 4.2: Local position (left) and velocity (right) profiles of the actuator trajectory. The position profile is given by (4.7) while the velocity is its first derivative. γ is the acceleration.

for $t[k] < t \leq t[k+1]$, γ denoting the actuator *acceleration*. At time $t = t_u[k+1]$, the actuator position (velocity, resp.) is equal to $s_u[k+1]$ ($\dot{s}_u[k+1]$, resp.), see Fig. 4.2. The gray dots on Fig. 4.1 illustrate the steady-state behavior of this control law when the parameters are tuned to match the ball position, velocity and acceleration at impact with the two control laws presented in Section 4.2.1.

The quadratic parameterization of the control (4.7) is convenient to obtain an explicit expression of the impact times: $t[k+1]$ is indeed the solution of (3.4) and (4.7) at time $t = t[k+1]$, which defines a second order polynomial in t . The controller inputs are $t_u[k+1]$ (4.5), $s_u[k+1] = s_\rho[k+1]$ and $\dot{s}_u[k+1]$ (4.6) and are functions of the state $(s[k], v[k])$ and impact time $t[k]$. Deadbeat convergence of this tracking control law, that is, convergence of the solution to the reference trajectory after a finite number of time steps, is established in the next section.

4.2.4 Deadbeat convergence

Substituting (4.4), (4.5) and (4.6) into (4.7) at time $t = t[k+1]$, we find:

$$\begin{aligned}
 s[k+1] &= s_\rho[k+1] \\
 &+ \frac{v_\rho[k+1] - e\sqrt{v[k]^2 - 2g(s_\rho[k+1] - s[k])}}{1+e} \left(t[k+1] - t[k] - \frac{v[k] + \sqrt{v[k]^2 - 2g(s_\rho[k+1] - s[k])}}{g} \right) \\
 &+ \frac{\gamma}{2} \left(t[k+1] - t[k] - \frac{v[k] + \sqrt{v[k]^2 - 2g(s_\rho[k+1] - s[k])}}{g} \right)^2. \tag{4.8}
 \end{aligned}$$

Substituting (3.6) into (4.8), we obtain a second order polynomial in $t[k+1]$, whose positive root is:

$$t[k+1] = t[k] + \frac{v[k] + \sqrt{v[k]^2 - 2g(s_\rho[k+1] - s[k])}}{g}. \tag{4.9}$$

Comparing this with (3.6) yields:

$$s[k + 1] = s_\rho[k + 1] \quad (4.10)$$

and therefore also:

$$v[k + 1] = v_\rho[k + 1] \quad (4.11)$$

$$t[k + 1] = t_u[k + 1] \quad (4.12)$$

reflecting then that the positive solution of (3.4), (3.5) and (4.7) is the exact matching between the reference and the real impact state.

To summarize, the continuous-time control law determined by the quadratic expression (4.7) and the discrete control (4.4), (4.5) and (4.6), ensures deadbeat convergence of the impact state after one time step. So far, the acceleration γ in (4.7) is a *free* parameter and does not influence the convergence. The control law is a *tracking* controller, that is, the reference trajectory $(s_\rho[\bullet], v_\rho[\bullet])$ is arbitrary, as long as it corresponds to a solution of the dynamical system (3.4) and (3.5).

4.2.5 Output feedback deadbeat control

The piecewise quadratic control proposed in Section 4.2.3 uses the full state $(s[k], v[k])$ of the system (3.4) and (3.5). To reduce the sensing requirements of the controller, we now assume that only the continuous-time actuator motion $s(t)$ is measured, together with the *impact times* $t[k]$: they provide the impact position $s[k]$ and velocity $\dot{s}[k]$. In this section, we derive a deadbeat *observer* that reconstructs the post-impact ball velocity $v[k]$ from the measured impact times $t[k]$ and actuator motion $s(t)$.

Post-impact velocity is estimated by an observer that is a copy of the velocity dynamics (3.5):

$$\hat{v}[k] = -e v[k - 1] + e g (t[k] - t[k - 1]) + (1 + e)\dot{s}[k] \quad (4.13)$$

while $v[k - 1]$ is obtained from (3.4):

$$\begin{aligned} \hat{v}[k] &= -e \left(\frac{s[k] - s[k - 1]}{t[k] - t[k - 1]} + \frac{g}{2}(t[k] - t[k - 1]) \right) + e g (t[k] - t[k - 1]) + (1 + e)\dot{s}[k] \\ &= e \frac{g}{2}(t[k] - t[k - 1]) - e \frac{s[k] - s[k - 1]}{t[k] - t[k - 1]} + (1 + e)\dot{s}[k]. \end{aligned} \quad (4.14)$$

Equation (4.14) defines a deadbeat velocity observer using the *impact times* as sole input in addition to the actuator motion. Deadbeat convergence is ensured in one time-step since $\hat{v}[k] = v[k]$, $\forall k > 1$.

The output feedback controller, whose the only measured signals are the *impact times*, is then obtained by replacing the actual state variable $v[k]$ by the estimated variable $\hat{v}[k]$ in (4.4), (4.5) and (4.6). Its deadbeat convergence is established in the following proposition:

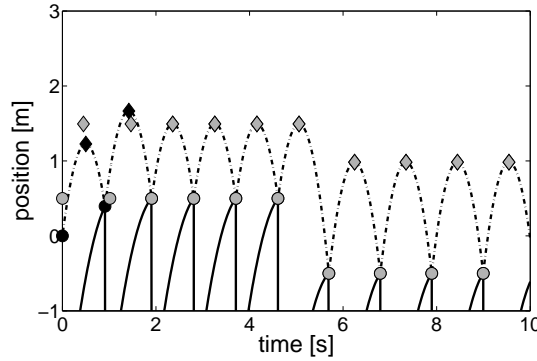


Figure 4.3: Output feedback control of the bouncing ball with the control law (4.15). The actuator (respectively the ball) position is depicted with solid (respectively dash-dotted) lines over time. Actual impacts position (apex position, resp.) are represented with black circles (black diamonds, resp.). Reference positions are accordingly represented with gray markers. $e = 0.7$, $\gamma < 0$.

Proposition 1 (Deadbeat convergence of the piecewise quadratic output feedback controller) *Consider the bouncing ball dynamics (3.4) and (3.5) and a reference trajectory $(s_\rho[k], v_\rho[k])$, $k \geq 0$. The output feedback control*

$$\begin{aligned}
 s(t) &= s_\rho[k+1] + \dot{s}_u[k+1](t - t_u[k+1]) + \frac{\gamma}{2}(t - t_u[k+1])^2 \\
 &\quad \text{for } t[k] < t \leq t[k+1] \\
 t_u[k+1] &= t[k] + \frac{\hat{v}[k] + \sqrt{\hat{v}[k]^2 - 2g(s_\rho[k+1] - s[k])}}{g} \\
 \dot{s}_u[k+1] &= \frac{v_\rho[k+1] - e\sqrt{\hat{v}[k]^2 - 2g(s_\rho[k+1] - s[k])}}{1+e} \\
 \hat{v}[k] &= e\frac{g}{2}(t[k] - t[k-1]) - e\frac{s[k] - s[k-1]}{t[k] - t[k-1]} + (1+e)\dot{s}[k] \quad (4.15)
 \end{aligned}$$

ensures deadbeat convergence of the 1D bouncing ball state toward the reference $(s_\rho[k], v_\rho[k])$ after two impacts (i.e. $k > 2$).

Proof The first impact is required to ensure convergence of the observer, since $\hat{v}[k] = v[k]$, $\forall k > 1$. As soon as $\hat{v}[k] = v[k]$, a second impact is required to achieve deadbeat convergence of the controller, as shown in Section 4.2.4. \square

The deadbeat convergence is illustrated in Fig. 4.3. At the third impact, both the reference impact position and the reference apex (which is an image of the reference post-impact velocity) are reached. The same figure illustrates the proper tracking of time-varying references since both the position and velocity references change at the seventh impact.

4.2.6 A blind mirror law based on output feedback

Assuming a ballistic flight between two impacts, the mirror law (3.18) can also be adapted to an *output* feedback control, with the impact times as measured output:

$$s(t) = \left(\frac{-(1-e)}{1+e} - \kappa_1 \left(E_\rho^* - \hat{E}(t) \right) \right) \hat{\beta}(t) \quad (4.16)$$

since both the ball position and energy can be estimated from impact state:

$$\begin{aligned} \hat{\beta}(t) &= s[k] + \hat{v}[k](t - t[k]) - \frac{g}{2}(t - t[k])^2 \\ \hat{E}(t) &= \hat{E}[k] \\ &= gs[k] + \frac{1}{2}\hat{v}[k]^2 \end{aligned}$$

for $t[k] \leq t < t[k+1]$. The tracking mirror law (3.18) requires a permanent tracking of the ball as sensory input. In contrast, the blind mirror law (4.16) based on output feedback only uses impact times and reconstructs the post-impact velocity $v[k]$ via the observer described in Section 4.2.5.

Since both the piecewise quadratic law (4.15) and the blind mirror law (4.16) require the same sensing capabilities, their robustness will be compared in the next section.

4.3 Robustness to Model Uncertainties

The *acceleration* parameter γ appearing in (4.15) played no role in the stability and convergence analysis. This section stresses the importance of this parameter for robustness purposes. We show that particular negative accelerations efficiently optimize either static or dynamical perturbations induced by a poor estimate of the coefficient of restitution e .

4.3.1 Uncertainty of the impact model

Among the several sources of uncertainty of the model (3.4) and (3.5), the *impact* model (3.3) is probably central. While the Newton impact law models e as a constant, this parameter is varying in experimental conditions. Furthermore, the linear relationship between the pre- and post-impact velocities (3.3) is certainly not respected outside a narrow range of impact velocities.

We model the uncertainty on the coefficient of restitution e by considering the following perturbed impact rule:

$$v[k+1] - \dot{s}[k+1] = -(e + \Delta e[k+1])(v^-[k+1] - \dot{s}[k+1]) \quad (4.17)$$

where $\Delta e[k+1]$ models the variation of the coefficient of restitution at time $t[k+1]$, w.r.t. the estimated value e . For the sake of simplicity, we study the robustness of the linearized feedback system, as derived in Appendix 4.A of this chapter.

From the linear state-space representation (4.28), we find the following closed-loop input-to-state transfer functions:

$$S(z) = S_\rho(z) + \frac{2(1-e)}{1+e} \frac{1}{z} E(z) \quad (4.18)$$

$$V(z) = V_\rho(z) + \frac{2}{1+e} \frac{z + \left(e^2 + \frac{\gamma}{g}(1+e)^2\right)}{z} E(z) \quad (4.19)$$

where $S(z)$, $V(z)$, $S_\rho(z)$, $V_\rho(z)$ and $E(z)$ refer to the z -transforms of $g\delta s[k]/(v_\rho^*)^2$, $\delta v[k]/v_\rho^*$, $g\delta s_\rho[k]/(v_\rho^*)^2$, $\delta v_\rho[k]/v_\rho^*$ and $\Delta e[k]$, respectively. In (4.18) and (4.19), the absence of dynamics in the transfer from references to states is due to the dead-beat convergence established in Section 4.2.5. The next section details the role of acceleration to reject the perturbations due to $\Delta e[k]$.

4.3.2 Robustness requires negative acceleration

From (4.19), we see that the acceleration γ can be designed to *place the zero* of the transfer function from $E(z)$ to $V(z)$. That design parameter will be discussed to optimize either the static or the dynamic performance.

Static error

To let the post-impact velocity converge toward the reference $v_\rho[k]$, assuming a *constant* perturbation $\Delta e[k] = \Delta e$, one has to cancel the static gain of the transfer function from $E(z)$ to $V(z)$. This amounts to place the zero of (4.19) at $z = -1$, which requires the following acceleration:

$$\gamma_{\text{stat.}} = -\frac{1+e^2}{(1+e)^2} g. \quad (4.20)$$

Interestingly, this optimal acceleration depends only on e , that is, the *estimated* coefficient of restitution. Fig. 4.4 illustrates the behavior of the feedback system when the coefficient of restitution is estimated at $e = 0.7$ while the real one is only $e + \Delta e = 0.5$. The desired post-impact velocity is reached because the difference between impact and apex positions is the same for the reference as for the actual trajectory. It should be noticed, however, that a static error persists on the reference position: the static gain from $E(z)$ to $S(z)$ is indeed independent of γ (see (4.18)). This static error does not appear to be detrimental to the robustness of the feedback system.

The optimal acceleration for static performance, as identified in (4.20), has also been derived from the original nonlinear equations, see Ronsse and Sepulchre (2006).

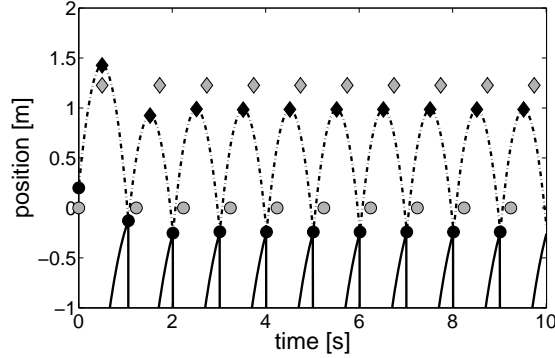


Figure 4.4: Output feedback control of the bouncing ball with piecewise quadratic trajectory. The actuator (ball, resp.) position is depicted with solid (dash-dotted, resp.) lines over time. Actual impacts position (apex position, resp.) are denoted with black circles (black diamonds, resp.). Reference positions are accordingly denoted with gray markers. $e + \Delta e = 0.5$, $e = 0.7$, γ is given by (4.20).

It is of interest to relate this particular acceleration to the sinusoidal control discussed in Section 4.2.1: the optimal acceleration (4.20) is exactly the middle point of the acceleration range where the period-one motion is stable (3.19).

Dynamic performance

Robustness to a static error on e is not the primary issue in real experiments because the average value of e is easy to determine. In contrast, robustness is required against the sustained variability of e . By placing the zero of (4.19) at $z = 0$, the dynamics from $E(z)$ to $V(z)$ are exactly canceled :

$$\gamma_{\text{dyn.}} = -\frac{e^2}{(1+e)^2}g \quad (4.21)$$

resulting in a static transfer function. Interestingly, this optimal value closely matches the value that minimizes the numerically computed variability of the sinusoidally actuated bouncing ball in Sternad et al. (2001a,b).

We summarize the robustness analysis of the piecewise quadratic law (4.15) with the following proposition:

Proposition 2 *Consider the bouncing ball dynamics (3.4) and (3.5) with a time-varying coefficient of restitution $e + \Delta e[k + 1]$. Using the output feedback control (4.15), the transfer function from $\Delta e[k]$ to $\delta v[k]/v_p^*$ is given by*

$$\frac{V(z)}{E(z)} = \frac{2}{1+e} \frac{z + \left(e^2 + \frac{\gamma}{g}(1+e)^2 \right)}{z}. \quad (4.22)$$

The choice $\gamma_{\text{stat.}} = -(1 + e^2)/(1 + e)^2 g$ (see (4.20)) ensures zero steady state error while the choice $\gamma_{\text{dyn.}} = -e^2/(1 + e)^2 g$ (see (4.21)) cancels the transfer function dynamics. Both choices result in negative acceleration at impact, with

$$\gamma_{\text{stat.}} < \gamma_{\text{dyn.}} \leq 0. \quad (4.23)$$

Simulation results

To illustrate the role of the impact acceleration for robustness in the nonlinear dynamics, we now compare the output piecewise quadratic controller (with the optimal negative accelerations previously identified) with the output controller mirror law (4.16). We have tested that $\kappa_1 \approx 0.025$ achieves the best trade-off between performance (rate of convergence) and robustness (noise sensitivity) in that blind mirror law.

Both the parabolic flight assumption and the Newton impact rule are perturbed by noise in an experimental setup. We simulated these perturbations by adding some noise to the reconstructed velocity $\hat{v}[k]$, whose dynamics use both the flight map and the impact rule. Equation (4.14) is thus replaced by:

$$\hat{v}[k] = \left(e \frac{g}{2} (t[k] - t[k-1]) - e \frac{s[k] - s[k-1]}{t[k] - t[k-1]} + (1 + e) \dot{s}[k] \right) (1 + \nu[k] \epsilon_{nl}) \quad (4.24)$$

where $\nu[k]$ is a random number between -1 and 1 , and ϵ_{nl} is the noise level. For the sake of illustration, we focus on stabilization of a period-one motion, characterized by $(s_\rho^*, v_\rho^*) = (0, g/2)$, i.e. one impact per second.

Fig. 4.5 depicts the standard deviation of the normalized post-impact velocity $v[k]/v^*$ over 100 impacts, for increasing noise level. The standard deviation of the impact *position* does not vary significantly depending on the control law, as suggested by (4.18). However, the piecewise quadratic law with the acceleration tuned to cancel the dynamics in (4.22) (γ defined by (4.21)) achieves quasi-zero variance in *post-impact velocity*, see the dashed line. For the tested noise levels, the standard deviation is intermediate with $\gamma = 0$. In contrast, both the blind mirror law and the piecewise quadratic law with γ defined by (4.20) generate twice as much variability. The excellent noise rejection obtained with $\gamma_{\text{dyn.}}$ (4.21), even considering the nonlinear dynamics, illustrates the robustness of the piecewise quadratic control law with a suitable negative acceleration. The range of negative acceleration that produces good noise rejection is obviously limited, since the more negative value $\gamma_{\text{stat.}}$ already results in poor dynamical performance.

4.3.3 Integral feedback control

The control objective considered in the previous sections was to track the position and velocity references (s_ρ^*, v_ρ^*) . However, as illustrated in Section 4.3.2, it is tedious to exactly cancel the static error of the post-impact velocity in the presence of model

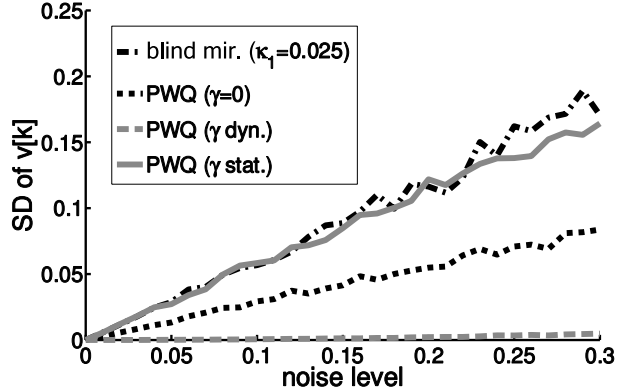


Figure 4.5: Simulations of the nonlinear noisy bouncing ball dynamics with different control laws: the blind mirror law (4.16) ($\kappa_1 = 0.025$, black dash-dotted), the zero-acceleration piecewise quadratic law (4.15) ($\gamma = 0$, black dotted), the piecewise quadratic law (4.15) with the optimal static acceleration (4.20) (gray plain) and the piecewise quadratic law (4.15) with the optimal dynamic acceleration (4.21) (gray dashed). The figure represents the standard deviation of the normalized post-impact velocity $v[k]/v^*$, calculated over 100 impacts. Noise level is defined in (4.24).

uncertainties. Given (3.8), the post-impact velocity static error will result in *flight time* static error (i.e. pattern frequency). This static error causes a linearly growing phase shift between the reference and the actual *impact times*, with detrimental consequences for pattern stabilization.

The velocity static error can be eliminated by integral feedback: the reference trajectory is now the position $s_\rho[\bullet]$ and the *impact time* $t_\rho[\bullet]$ (i.e. impact phase). The corresponding velocity input $v_\rho[k+1]$ in $\dot{s}_u[k+1]$ (4.15) is computed as the solution of (3.6):

$$v_\rho[k+1] = \frac{s_\rho[k+2] - s_\rho[k+1]}{t_\rho[k+2] - t_u[k+1]} + \frac{g}{2}(t_\rho[k+2] - t_u[k+1]). \quad (4.25)$$

The difference between the *reference* impact time $t_\rho[k+2]$ and the *estimated* impact time $t_u[k+1]$ must be then constant in steady-state:

$$(t_\rho[k+1] - t_u[k])^* = \frac{2v_\rho^*}{g}. \quad (4.26)$$

Since the difference between the estimated and the actual impact times is also a constant in steady-state, the delay between the reference and the actual impact times will remain constant through impacts, resulting in no static error between the desired and actual post-impact velocity, and therefore in the pattern frequency.

Deadbeat convergence in three impacts of the integral controller is straightforwardly established by adapting the derivations of Section 4.2.3. Note that this

controller requires reference signals *two* steps ahead since both $s_\rho[k+2]$ and $t_\rho[k+2]$ are used in (4.25).

4.4 Conclusion

This chapter presented the design, analysis and simulations of robust closed-loop control of the period-one motion in the bouncing ball. The control law only uses the impact times as feedback information, relaxing thereby the need for complex sensor design. The parameter γ , i.e. the acceleration at impact, plays no role in the stability analysis; in contrast, proper tuning of this parameter was shown to have a dramatic effect on robustness. The design is based on the simple Newton's impact model and we model the uncertainty by treating the variations of the coefficient of restitution as an external disturbance. Analyzing the transfer function from this disturbance to the impact velocity, we showed that the dynamics can be exactly canceled by a proper choice of the impact acceleration. This particular tuning requires *negative* impact acceleration, in accordance with sensorless control strategies (Holmes, 1982; Schaal et al., 1996; Ronsse et al., 2006) and with observed human strategies (Schaal et al., 1996; Sternad et al., 2001a,b). This contrasts with the mirror law algorithm proposed earlier in the literature (Buehler et al., 1988, 1990, 1994) and possibly explains why such control schemes — that have been shown to perform robustly in 1D, 2D and even 3D environments with a continuous-time sensing of the juggled object — may perform poorly in implementations with limited sensing capabilities (Gerard, 2005).

The chapter illustrated that measurement of impact times is both a cheap and relevant feedback source in juggling experiments. It may therefore supplement the continuous-time sensing required in more complicated juggling implementations, e.g. in 3D environments. The piecewise quadratic control introduced in the present chapter will be generalized to a smoother closed-loop trajectory in Chapter 7. This will permit to validate this strategy on a real experimental setup.

The results of the present chapter have been published in Ronsse et al. (2007a), Sections II to IV.

4.A Linearized Equations of the 1D Noisy Bouncing Ball with Piecewise Quadratic Control

The linearized dynamics of the perturbed 1D bouncing ball dynamics (3.4) and (4.17), and the piecewise quadratic law (4.15) are given by the following set of equations:

$$\begin{aligned}
 \delta s[k+1] &= \delta s[k] + \frac{2\pi n}{\omega} \delta v[k] - \frac{\pi n g}{\omega} (\delta t[k+1] - \delta t[k]), \\
 \delta v[k+1] &= -e \delta v[k] + e g (\delta t[k+1] - \delta t[k]) + (1+e) \delta \dot{s}[k+1] \\
 &\quad + \frac{2}{1+e} \frac{\pi n g}{\omega} \delta e[k+1], \\
 \delta s[k+1] &= \frac{2e}{1+e} \delta s_\rho[k+1] + \frac{1-e}{1+e} \delta s[k] \\
 &\quad + \frac{1-e}{1+e} \frac{\pi n g}{\omega} (\delta t[k+1] - \delta t[k]) - \frac{1-e}{1+e} \frac{2\pi n}{\omega} \delta \hat{v}[k], \\
 \delta \dot{s}[k+1] &= \frac{1}{1+e} \delta v_\rho[k+1] - \left(\frac{e}{1+e} + \frac{2\gamma}{g} \right) \delta \hat{v}[k] \\
 &\quad + \left(\frac{e}{1+e} + \frac{\gamma}{g} \right) \frac{\omega}{\pi n} (\delta s_\rho[k+1] - \delta s[k]) + \gamma (\delta t[k+1] - \delta t[k]), \\
 \delta \hat{v}[k+1] &= e \frac{g}{2} (\delta t[k+1] - \delta t[k]) - e \frac{\omega}{2\pi n} (\delta s[k+1] - \delta s[k]) + (1+e) \delta \dot{s}[k+1].
 \end{aligned} \tag{4.27}$$

In (4.27), $\delta e[k+1]$ is the small perturbation on the coefficient of restitution and is considered as an additional input.

Using non-dimensional state variables, one obtains the following state-space model:

$$\begin{aligned}
 \begin{pmatrix} \frac{g\delta s[k+1]}{(v_\rho^*)^2} \\ \frac{\delta v[k+1]}{v_\rho^*} \\ \frac{g\delta t[k+1]}{v_\rho^*} \\ \frac{\delta \hat{v}[k+1]}{v_\rho^*} \end{pmatrix} &= \underbrace{\begin{pmatrix} 0 & 1-e & 0 & -(1-e) \\ 0 & e^2 + \frac{\gamma}{g}(1+e)^2 & 0 & -\left(e^2 + \frac{\gamma}{g}(1+e)^2\right) \\ 1 & 1+e & 1 & 1-e \\ 0 & e^2 + \frac{\gamma}{g}(1+e)^2 & 0 & -\left(e^2 + \frac{\gamma}{g}(1+e)^2\right) \end{pmatrix}}_{\mathbf{A}'} \begin{pmatrix} \frac{g\delta s[k]}{(v_\rho^*)^2} \\ \frac{\delta v[k]}{v_\rho^*} \\ \frac{g\delta t[k]}{v_\rho^*} \\ \frac{\delta \hat{v}[k]}{v_\rho^*} \end{pmatrix} \\
 &\quad + \underbrace{\begin{pmatrix} 1 & 0 & 0 \\ 0 & 1 & \frac{2}{1+e} \\ -1 & 0 & 0 \\ 0 & 1 & 0 \end{pmatrix}}_{\mathbf{B}'} \begin{pmatrix} \frac{g\delta s_\rho[k+1]}{(v_\rho^*)^2} \\ \frac{\delta v_\rho[k+1]}{v_\rho^*} \\ \delta e[k+1] \end{pmatrix}. \tag{4.28}
 \end{aligned}$$

The state variables are small perturbations of the ball impact position $g\delta s[k+1]/(v_\rho^*)^2$ and velocity $\delta v[k+1]/v_\rho^*$; the impact time $g\delta t[k+1]/v_\rho^*$ and the observed velocity $\delta \hat{v}[k+1]/v_\rho^*$.

The matrix \mathbf{A}' is singular. This is a consequence of deadbeat convergence of the 1D bouncing ball, controlled with the piecewise quadratic law (4.15).

Chapter 5

Experimental Setup: the Wiper Robot

To be intelligent is to be
open-minded, active, memoried,
and persistently experimental.

Leopold Stein

5.1 Introduction

At the center of the thesis, this chapter describes the experimental setup we designed to conduct robotics and motor control experiments on impact juggling. One major contribution of the present work was to design this experimental setup, amenable to test both the theoretical predictions in robotics and to explore the human behavior. This setup is based on a simplified juggling paradigm, both capturing the main features of regular juggling, and amenable to simple mathematical modeling. This setup is described in Section 5.2, such as a crude model which is shown to be reducible to the bouncing ball model described in Chapter 3.

More technical details on the setup are given in Appendix B.

5.2 Wiper: an experimental setup amenable to mathematical modeling

One of the most popular juggling patterns is called the shower, and is depicted in Fig. 5.1(a): the balls follow a cyclic trajectory along two distinct parabolas produced by a low and a high toss. We study this steady-state pattern in an experiment that drastically simplifies the hardware: a *planar* motion of the puck between two impacting edges that idealize the juggler's arms. Fig. 5.1(b) depicts the so-called

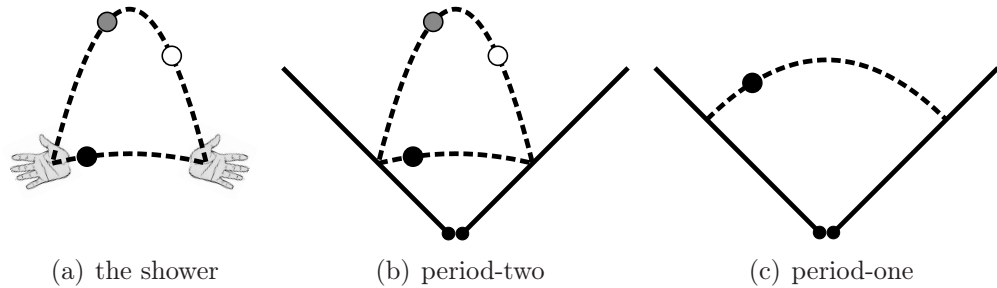


Figure 5.1: The *shower* pattern (Fig. 5.1(a)) is one of the simplest juggling pattern. It corresponds to a limit cycle of Wiper that is called the *period-two* (Fig. 5.1(b)), since the balls cycle between the edges along two parabolas. A degenerate (and simpler) case of the period-two, where both parabolas are similar, is called the *period-one* (Fig. 5.1(c)).

period-two orbit of this impact juggler, and the particular period-one orbit (both tosses are equal) is depicted in Fig. 5.1(c).

Laboratory implementation of this impact juggling experiment has been realized on the *Wiper* robot, pictured in Fig. 5.2. The motion plane is a tilted air-hockey table. Air-hockey is a popular game which is based on tight goal-shots of plastic pucks on an horizontal table. The puck trajectories are almost frictionless since the table is pierced with a lattice of little holes blowing air constantly. This frictionless table has been tilted with respect to the ground, such that gravity influences the puck motion, like in regular juggling. The gravity field \mathbf{g} can be adjusted by proper inclination of the table. The two metallic “arms” have a single (rotational) degree of freedom. The pucks have been manufactured from hertalon, a nylon derivative that is both light and elastic.

Wiper is tunable to different configurations (angle of inclination, sensors design, actuation level) and easy to instrument. The edges can indeed be directly actuated by two DC motors, as depicted in Fig. 5.2. The setup has been used to study the stabilization of simple periodic orbits in impact juggling, such as the period-one and the period-two depicted in Fig. 5.1.

Wiper can also be rapidly adapted to study human juggling. Replacing the motors by free rotational joints, human subjects can indeed actuate the edges through direct catching (see Fig. 5.3). The stabilization of the period-one juggling task (Fig. 5.1(c)) is easy and fast to learn. Wiper allows to test this stabilization task at different tempi, since the flight time between two impacts depends on the steady-state angle between the two edges. If the angle is large, the tempo will be slow, and vice-versa. In principle, this setup is also suitable to study more complex patterns, e.g. the period-two (Fig. 5.1(b)). This would permit to focus on learning issues and/or feedback selection issues, since the subjects would not be able to keep several pucks in visual tracking at the same time.



Figure 5.2: Picture of Wiper.

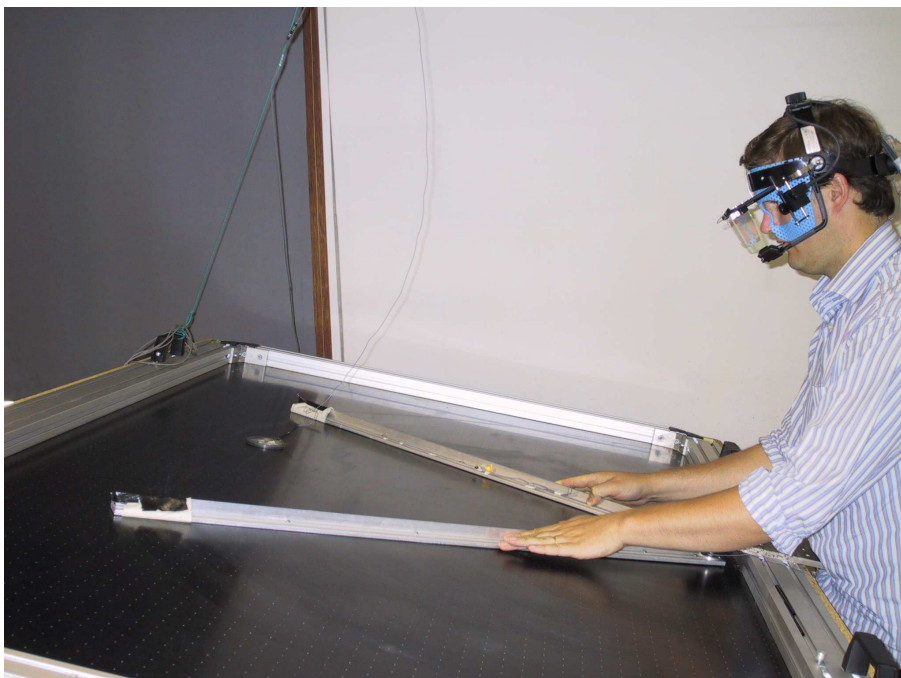


Figure 5.3: Wiper can be actuated by human subjects.

Wiper is also amenable to simple *mathematical modeling*. Similarly to the bouncing ball dynamics (see Section 3.2), the dynamical model consists of planar flight phases separated by impacts:

- (a) during flight phases, the juggled puck trajectories are ballistic flights along a parabola, solution of the Newton's equation $d^2\vec{p}/dt^2 = -\vec{g}$:

$$\begin{aligned} p_{\perp}(t) &= p_{\perp}[k] + v_{\perp}[k]t, \\ p_{//}(t) &= p_{//}[k] + v_{//}[k]t - 0.5gt^2 \end{aligned} \tag{5.1}$$

with $(p_{\perp}[k], p_{//}[k])$ and $(v_{\perp}[k], v_{//}[k])$ denoting the impact position and velocity at impact k , orthogonal and parallel to the gravity field, respectively;

- (b) at impact, there is a sharp discontinuity in the velocity profile. We model the impact with the simplest Newton's law:

$$\begin{aligned} v_n^+ - \dot{s}_n &= -e(v_n^- - \dot{s}_n), \\ v_t^+ - \dot{s}_t &= v_t^- - \dot{s}_t \end{aligned} \tag{5.2}$$

where (v_n^-, v_t^-) and (v_n^+, v_t^+) are the normal and tangential components of the velocity, with respect to the impacting surface, before and after the impact, respectively; and (\dot{s}_n, \dot{s}_t) are the impactor velocity at impact, in the normal and tangential directions w.r.t. the impacting surface. In (5.2), the normal equation is obviously exactly equivalent to (3.3).

The coefficient of restitution $0 \leq e \leq 1$ still models the dissipated energy at impact. The impact model is only a crude approximate of real impact dynamics, since for example it does not capture spin effects of the puck at impact (Spong, 2001). The complete dynamics of Wiper under these simplifying assumptions has been derived in previous papers (Sepulchre and Gerard, 2003; Gerard and Sepulchre, 2005; Ronsse et al., 2007a, 2006) and is derived in the next chapter of this thesis.

A further simplification of Wiper's dynamics is of interest to connect the model with the popular 1D bouncing ball model, studied in Section 3.2 (Holmes, 1982; Guckenheimer and Holmes, 1986; Bapat et al., 1986). Assuming an orthogonal wedge angle and parallel actuations of the edges (that is, the two edges are assumed to remain aligned with the two orthogonal axes of Fig. 5.4), the 2D motion of the juggled objects projects on each axis to a 1D motion that is unaffected by the bounces on the other axis (Sepulchre and Gerard, 2003; Ronsse et al., 2007a), see Fig. 5.4. In this special configuration, a period-two pattern in Wiper corresponds to two frequency-locked period-one bouncing ball patterns (i.e. constant bounce height, see Fig. 3.2) along the axes. The *phase* relationship between those two patterns determines biunivocally the shape of the periodic orbit. The period-one orbit corresponds to two balls bouncing exactly in anti-phase (i.e. one is at the apex when the other bounces). The period-two patterns correspond to any other phase relationship.

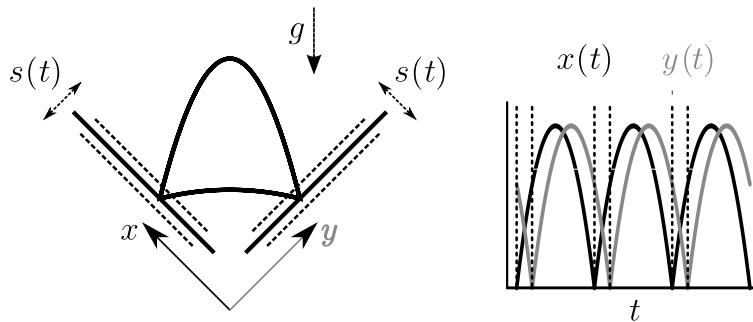


Figure 5.4: A special configuration of the wedge planar juggler that decouples the 2D ball motion (left) into two independent 1D bouncing ball motions (right). The right frame represents the ball trajectories over time along the x and y axes.

5.3 Conclusion

The *Wiper* has been designed from a simplified juggling experiment, aiming at mimicking one of the most popular juggling patterns — i.e. the shower — through its periodic orbits.

A further simplified model of *Wiper*'s dynamics reduces to the bouncing ball dynamics. Its stability properties can consequently be directly inherited from the bouncing ball ones, that are described in Section 3.2. The simplified model is useful to capture in a simple way the main properties of *Wiper*'s periodic orbits. It has been instrumental to develop modeling and design investigations discussed in the next chapters.

This chapter material has been partly published in Ronsse et al. (2007a, 2006, 2007b).

Chapter 6

Sensorless Stabilization of 2D Patterns of the Wiper Robot

Remember that there is nothing
stable in human affairs;
therefore avoid undue elation in
prosperity, or undue depression
in adversity.

Socrates

6.1 Introduction

The goal of the present chapter is to characterize a general model of Wiper's dynamics, their periodic orbits, and their *open-loop* stability properties. Indeed, since a crude approximation of Wiper's dynamics reduces to the bouncing ball model (see Section 5.2), it is sounded to investigate whether the mere sinusoidal actuation (3.7) also stabilizes some periodic pattern in our 2D juggling setup.

The control studied in this chapter is then a sinusoidal actuation of the edges, perhaps the simplest imitation of the fundamental cyclic motion of the hands of a juggler. Sinusoidal motion is also the simplest output of the oscillating circuits that have been used so far for modeling rhythmic movements (see Section 2.1.4). The vibration *frequency* of the edges is the key parameter since the stabilization mechanism rests on a synchronization (or frequency-locking) between the controller and the tempo of the juggling pattern. The vibration *amplitude* is a critical control parameter since the periodic orbits of Wiper are stable for a restricted amplitude range, as it was previously illustrated for the bouncing ball (3.17).

In this chapter, we describe the dynamics of a wedge-billiard, as a mathematical model of the Wiper planar juggler. This model is valid at any wedge angle, while the simplified version derived in Section 5.2 was restricted to the square configuration ($\theta = 45^\circ$). We analyze the existence and stability of periodic orbits of the

wedge-billiard. The chapter main result is to show that some exponentially unstable periodic orbits of the elastic model are stabilized in the non-elastic model with the sinusoidal control that uses no feedback measurement, hence the name *sensorless stabilization*, and to provide an experimental validation of this result. The result somewhat contradicts the intuition that the stabilization of unstable steady-states normally involves feedback. For the period-one orbit also discussed in this chapter, the result has been previously observed by Schaal and Atkeson (1993), at least numerically, who reported the planar juggler as one example of rhythmic system that can be stabilized without feedback.

Section 6.2 presents the wedge-billiard model and outlines some limitations of this model with respect to the expected real Wiper dynamics. In Section 6.3, the steady-state solutions of this model are derived. They correspond to fixed points of the iteration map, and therefore to periodic orbits of the wedge-billiard. In the unactuated, elastic ($e = 1$) wedge-billiard, none of these periodic orbits are stable.

These periodic orbits can nevertheless be stabilized through sinusoidal actuation. First this is demonstrated in Section 6.4 by considering parallel actuations of the edges. As mentioned in Section 5.2, this problem reduces to the analysis of bouncing ball dynamics in the square configuration ($\theta = 45^\circ$). Then the stability properties are straightforwardly inherited. In Section 6.5, the model is further generalized to account for the rotational actuation of the edges. The expected parametric stability region of Wiper are derived. Stability of the periodic orbits depends on the actuation amplitude A , the coefficient of restitution e , and — less intuitively — on the angle of impact θ . In particular, the periodic orbits that were all instable for $\theta > 45^\circ$ in the unactuated and elastic wedge-billiard, can be stabilized with the sensorless sinusoidal actuation.

Finally, Section 6.6 describes experimental validations of open-loop stabilization of Wiper's periodic orbits. The experimental parametric stability regions obtained with the setup described in Section 5.2 are compared with the theoretical parametric stability regions, derived in Section 6.5.

6.2 A bounce juggler model

The aim of the present section is to derive a crude mathematical model of the Wiper robot, presented in Chapter 5. This robot is an idealization of a human juggler. We consider a motion restricted to a plane under a constant gravitational field \mathbf{g} (with $|\mathbf{g}| = g$). The juggled ball undergoes collisions with two edges, which act as the juggler arms (see Fig. 6.1). In contrast with human juggler, the impacts between Wiper's edges and the ball are supposed to be instantaneous, hence the name *impact* (or *bounce*) juggling.

Our model is a control version of the model introduced by Lehtihet and Miller (1986) and was first presented by Sepulchre and Gerard (2003) in order to study several closed-loop *control* laws to stabilize impact juggling patterns. The four-

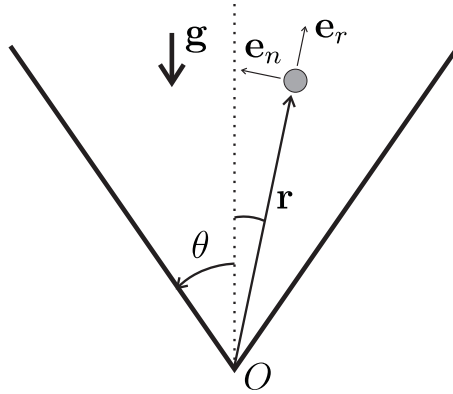


Figure 6.1: The wedge-billiard.

dimensional wedge-billiard dynamics are studied via the three-dimensional discrete Poincaré map relating the state *from one impact to the next one*, the ball motion between two impacts being parabolic (a ballistic flight in a constant gravitational field \mathbf{g}). Let $(\mathbf{e}_r, \mathbf{e}_n)$ be an orthonormal frame attached to the fixed point O with \mathbf{e}_r aligned with the ball position vector $\mathbf{r} = r\mathbf{e}_r$. The ball is assumed to be a unit mass point, let $\mathbf{v} = v_r\mathbf{e}_r + v_n\mathbf{e}_n$ denote its velocity. Therefore the discrete state vector denotes the state of the ball at impacts. This state being discontinuous at impacts, we choose the post-impact values to make up the state vector as a convention¹:

$$\mathbf{x}[k] \equiv \begin{pmatrix} V_r[k] \\ |V_n|[k] \\ R[k] \end{pmatrix} = \begin{pmatrix} V_r^+(t[k]) \\ |V_n^+(t[k])| \\ R^+(t[k]) \end{pmatrix}$$

where $V_r = v_r / \cos \theta$, $V_n = v_n / \sin \theta$ and $R = r / \cos \theta$ denote the state of the ball and the $\bullet^+[k]$ notations denote the post-impact values, evaluated at impact time $t[k]$. The corresponding pre-impact values are denoted $\bullet^-[k]$. We consider the absolute value of the normal velocity, the wedge-billiard being symmetric with respect to its bisecting line.

According to this state vector, the impact law of the wedge-billiard \mathcal{I} derives from (5.2):

$$\begin{aligned} V_r[k] &= V_r^-[k], \\ V_n[k] &= -eV_n^-[k] + (1+e)\dot{S}[k] \end{aligned} \tag{6.1}$$

where $\dot{S}[k] = \dot{S}(t[k]) = \dot{s}(t[k]) / \sin \theta$ and $\dot{s}(t[k])$ denotes the edge velocity at the impact time $t[k]$ and is consequently the system control input.

Assuming that the change in the edges position can be neglected to compute the ball flight map (this assumption rests basically on a *small amplitude* actuation

¹A similar choice has been made for the bouncing ball state vector, see Section 3.2.

of the edges, see the discussion in Section 6.5), the flight map is the velocity and position update of the ball integrated through a flight between two impacts on the *unactuated* wedge-billiard, i.e. (5.1). Two different flight maps must be considered whether these impacts occur on the same edge or not. These flight maps have been derived by Sepulchre and Gerard (2003). The rest of this thesis focusing only on solutions, and stability properties, where the ball hits the edges alternately, the wedge-billiard map \mathcal{B} is therefore the composition of the impact rule \mathcal{I} (6.1) and the second flight map (Lehtihet and Miller, 1986; Sepulchre and Gerard, 2003):

$$\begin{aligned} V_r^-[k+1] &= |V_n|[k] - V_r[k] - |V_n^-|[k+1], \\ |V_n^-|[k+1] &= \sqrt{\left(\frac{2V_r[k] + (\alpha^2 - 1)|V_n|[k]}{1 + \alpha^2}\right)^2 + \frac{4g}{1 + \alpha^2}R[k]} \end{aligned} \quad (6.2)$$

with

$$\alpha = \tan \theta.$$

One obtains the discrete billiard map \mathcal{B} :

$$\begin{aligned} V_r[k+1] &= |V_n|[k] - V_r[k] - |V_n^-|[k+1], \\ V_n[k+1] &= -e|V_n^-|[k+1] \operatorname{sign}(V_n[k]) + (1+e)\dot{S}[k+1], \\ R[k+1] &= R[k] - \frac{1}{2g}(V_r^2[k+1] - V_r^2[k]) - \frac{\alpha^2}{2g}(|V_n^-|^2[k+1] - V_n^2[k]). \end{aligned} \quad (6.3)$$

The position update of (6.3) derives from the *energy* expression:

$$E[k] = \frac{1}{1 + \alpha^2} \left(\frac{1}{2}V_r^2[k] + \frac{\alpha^2}{2}V_n^2[k] + gR[k] \right) \quad (6.4)$$

and the conservation of energy through the flight implies: $E^-[k+1] = E[k]$.

For later reference, one also notes the flight time, i.e. the time between two consecutive impacts, given by:

$$\begin{aligned} \Delta t[k] &\equiv t[k+1] - t[k] \\ &= \frac{1}{g} \left(|V_n^-|[k+1] + \frac{(\alpha^2 - 1)|V_n|[k] + 2V_r[k]}{1 + \alpha^2} \right). \end{aligned} \quad (6.5)$$

The wedge-billiard model \mathcal{B} (6.3) differs clearly from the actual Wiper dynamics. These differences are covered by the following mechanical assumptions:

1. The edges are not affected by the impacts, so that their velocity is continuous at impact times.
2. The impacts are localized in space around the fixed wedge (“small angle” assumption).
3. The contact is frictionless.

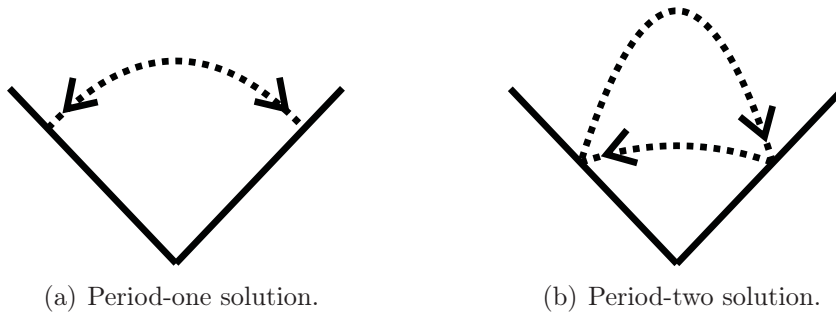


Figure 6.2: Two periodic orbits of the wedge-billiard. These periodic orbits are equivalent to Wiper’s periodic orbits, depicted in Fig. 5.1.

Assumption 1 relies on the fact that the edges are largely heavier than the puck. If the edges motors track a smooth reference signal, the perturbation caused at one impact time is rejected by the next impact time. Note that a finite mass ratio between the actuator and the object can be captured by a modified coefficient of restitution: Vincent and Mees (2000) studied a 1D bouncing ball model capturing this effect. The effect of assumption 2 is more tedious to analyse. Relaxing the “small angle” assumption leads to an implicit billiard map that is much more complicated to solve. Assumption 3 is reasonable. Friction at impacts induces the puck to *spin*. This leads to a more complicated model that will have topologically similar steady-state orbits. See the discussion in Section 6.6.2. The impact controllability of an air hockey puck has been studied by Spong (2001).

6.3 Energy balance of the steady-state solutions

One of the most common juggling patterns is called the *shower*. It involves a circle-shaped trip of several balls between the juggler hands (Fig. 5.1(a)). This section will describe and analyze a periodic solution of the model (6.3) which is very close to the shower pattern, i.e. the *period-two* orbit described in Chapter 5.

The first part of this section describes a degenerate case of the period-two orbits where both flight times are equal, i.e. the *period-one* orbit. The general period-two solution of the wedge-billiard will be investigated in Section 6.3.2. Stability properties of these solutions in the *unactuated elastic* wedge will be also investigated.

6.3.1 Period-one orbit

The period-one orbit is a round trip of the ball between the edges, both trajectories being exactly the same (Fig. 6.2(a)). Due to its symmetry, this periodic motion is characterized by a *unique* energy level E^* . The radial velocity V_r and the position R being conserved at impacts, the conservation of energy implies the conservation

of the square normal velocity:

$$(V_n^*)^2 = (V_n^{-*})^2. \quad (6.6)$$

Using (6.6), we obtain in the steady-state solution of (6.3):

$$V_r^* = |V_n^*| - V_r^* - |V_n^{-*}|, \quad (6.7)$$

$$|V_n^*| = e |V_n^{-*}| + (1 + e)|\dot{S}^*| \quad (6.8)$$

which implies $V_r^* = 0$. These results have a direct geometrical interpretation on Fig. 6.2(a): at the impacts, the radial velocity must be zero, and the normal velocity must be exactly reversed, for this steady-state motion. The steady-state edges velocity derives from (6.8):

$$|\dot{S}^*| = \frac{1 - e}{1 + e} |V_n^*|. \quad (6.9)$$

Using (6.4), (6.5) and (6.2), the fixed point of (6.3) is conveniently parametrized by the energy E^* :

$$|V_n^*| = \frac{1 + \alpha^2}{\alpha} \sqrt{\frac{2E^*}{3 + \alpha^2}}, \quad (6.10)$$

$$R^* = \frac{2(1 + \alpha^2)}{g(3 + \alpha^2)} E^*, \quad (6.11)$$

$$\Delta t^* = \frac{2\alpha}{g} \sqrt{\frac{2E^*}{3 + \alpha^2}}. \quad (6.12)$$

If the edges are elastic ($e = 1$), no energy supply is needed to sustain the period-one motion (see (6.9): $|\dot{S}^*| = 0$). This could be also simulated from a non-elastic wedge-billiard if the edges compensate for the energy dissipation at each impact: $|\dot{S}^*| = (1 - e)/(1 + e)|V_n^-|[k + 1]$.

Proposition 3 (see Lehtihet and Miller (1986)) *For every $\theta \in (0^\circ, 90^\circ)$ and for every energy level E^* , the wedge-billiard possesses a unique period-one orbit, determined by the fixed point (6.10), (6.11), (6.12) of the model (6.3). This orbit is marginally stable if $\theta < 45^\circ$ ($\alpha < 1$), unstable if $\theta = 45^\circ$ ($\alpha = 1$) and exponentially unstable if $\theta > 45^\circ$ ($\alpha > 1$).*

Proof Stability of the period-one orbits is investigated via the Jacobian linearization of (6.3) at the fixed point (6.10), (6.11), (6.12) which gives:

$$\begin{pmatrix} \delta V_r[k + 1] \\ \delta |V_n|[k + 1] \\ \frac{g}{|V_n^*|} \delta R[k + 1] \end{pmatrix} = \begin{pmatrix} \frac{1 - 4\alpha^2 - \alpha^4}{(1 + \alpha^2)^2} & \frac{4\alpha^2}{(1 + \alpha^2)^2} & \frac{-2}{1 + \alpha^2} \\ \frac{2(\alpha^2 - 1)}{(1 + \alpha^2)^2} & \frac{(\alpha^2 - 1)^2}{(1 + \alpha^2)^2} & \frac{2}{1 + \alpha^2} \\ \frac{2\alpha^2(1 - \alpha^2)}{(1 + \alpha^2)^2} & \frac{4\alpha^4}{(1 + \alpha^2)^2} & \frac{1 - \alpha^2}{1 + \alpha^2} \end{pmatrix} \begin{pmatrix} \delta V_r[k] \\ \delta |V_n|[k] \\ \frac{g}{|V_n^*|} \delta R[k] \end{pmatrix}. \quad (6.13)$$

The eigenvalues of this Jacobian matrix are:

$$\lambda_{1,2,3} = 1, \frac{1 - 4\alpha^2 - \alpha^4 \pm 2\alpha\sqrt{(\alpha^2 - 1)(\alpha^2 + 3)}}{(1 + \alpha^2)^2}. \quad (6.14)$$

One unitary eigenvalue ($\lambda_1 = 1$) is associated with the conservation of energy. The remaining two eigenvalues (λ_2 and λ_3) lie on the unitary circle for $\alpha < 1$, and it can be shown that the period-one solution is marginally stable in this case: in the state space plane of the elastic wedge-billiard, the period-one fixed point is surrounded by a continuum of closed orbits that correspond to *quasi-periodic* solutions (Lehtihet and Miller, 1986). When the wedge is a right angle ($\alpha = 1$), $\lambda_2 = \lambda_3 = -1$: the map \mathcal{B} has therefore an eigenvalue of algebraic multiplicity 2 on the unit circle. The unactuated wedge-billiard dynamics becoming *linear* in that case (see Sepulchre and Gerard, 2003), the period-one orbits are unstable. For $\alpha > 1$, the two eigenvalues are real, one of them being outside the unitary circle, the period-one solution is therefore exponentially unstable. \square

6.3.2 Period-two orbit

Period-two orbits model the shower juggling pattern presented in Fig. 5.1(a). The round trip of the ball between the edges is now characterized by two different trajectories depending on the direction of the ball. Fig. 6.2(b) is an example of a period-two solution. This solution will be characterized by two parameters E^{r^*} and E^{l^*} , associated to the ball energy on *each* trajectory, assuming arbitrarily that \bullet^{r^*} characterizes the right-edge impacts and \bullet^{l^*} the left-edge impacts. A positive edge velocity corresponds to a counterclockwise motion. The period-one orbit is a degenerate case of the period-two orbits for which $E^{r^*} = E^{l^*}$.

A period-two solution is characterized by two points in the state space, say \mathbf{x}^{r^*} and \mathbf{x}^{l^*} : these points ought to be fixed points of $\mathcal{B}^2 = \mathcal{B} \circ \mathcal{B}$. The position and the radial velocity being conserved at impact, the global energy balance of the period-two solution requires this time:

$$(V_n^{r^*})^2 - (V_n^{-r^*})^2 = - \left((V_n^{l^*})^2 - (V_n^{-l^*})^2 \right). \quad (6.15)$$

A possible loss of energy on one edge has to be compensated on the other one.

Eliminating the radial velocities $V_r^{r^*}$ and $V_r^{l^*}$ from their update equations:

$$V_r^{l^*} = |V_n^{r^*}| - V_r^{r^*} - |V_n^{-l^*}|, \quad (6.16)$$

$$V_r^{r^*} = |V_n^{l^*}| - V_r^{l^*} - |V_n^{-r^*}|, \quad (6.17)$$

we find another relation between the normal velocities:

$$|V_n^{r^*}| - |V_n^{-l^*}| = |V_n^{l^*}| - |V_n^{-r^*}|. \quad (6.18)$$

Equations (6.15) and (6.18) yield:

$$|V_n^{r^*}| + |V_n^{-l^*}| = -(|V_n^{l^*}| + |V_n^{-r^*}|). \quad (6.19)$$

Thanks to (6.18) and (6.19), one finds $|V_n^{-l^*}| = -|V_n^{l^*}|$ and $|V_n^{-r^*}| = -|V_n^{r^*}|$. These four variables being non-negative, (6.18) must be equal to zero to be satisfied, such as (6.15):

$$\begin{aligned} |V_n^{-l^*}| &= |V_n^{r^*}|, \\ |V_n^{-r^*}| &= |V_n^{l^*}|. \end{aligned} \quad (6.20)$$

The radial velocity and the impact position should then satisfy (see (6.16) and (6.3)):

$$V_r^{l^*} = -V_r^{r^*}, \quad (6.21)$$

$$R^{r^*} = R^{l^*} = R^*. \quad (6.22)$$

Geometrically, the period-two solutions are therefore characterized by two symmetrical parabolas: these parabolas reach their highest point (zenith) on the bisecting line of the wedge.

Introducing the normal velocity conservation (6.20) in (6.3), we obtain the steady-state relations:

$$\begin{aligned} |V_n^{l^*}| &= e|V_n^{r^*}| - (1+e)\dot{S}^{l^*}, \\ |V_n^{r^*}| &= e|V_n^{l^*}| + (1+e)\dot{S}^{r^*}. \end{aligned} \quad (6.23)$$

Equations (6.23) provide the steady-state edges velocities:

$$\begin{aligned} \dot{S}^{r^*} &= \frac{|V_n^{r^*}| - e|V_n^{l^*}|}{1+e}, \\ \dot{S}^{l^*} &= \frac{e|V_n^{r^*}| - |V_n^{l^*}|}{1+e}. \end{aligned} \quad (6.24)$$

Injecting (6.20) in the definitions of $|V_n^-|$, we find:

$$(V_n^{r^*})^2 = \left(\frac{2V_r^{r^*} + (\alpha^2 - 1)|V_n^{r^*}|}{1 + \alpha^2} \right)^2 + \frac{4g}{1 + \alpha^2} R^*, \quad (6.25)$$

$$(V_n^{l^*})^2 = \left(\frac{2V_r^{l^*} + (\alpha^2 - 1)|V_n^{l^*}|}{1 + \alpha^2} \right)^2 + \frac{4g}{1 + \alpha^2} R^* \quad (6.26)$$

which implies, taking (6.21) into account:

$$V_r^{r^*} = \frac{\alpha^2}{\alpha^2 - 1} (|V_n^{r^*}| - |V_n^{l^*}|) = -V_r^{l^*}. \quad (6.27)$$

The impact position and the energy levels are derived from (6.25), (6.27), (6.4) and (6.28):

$$R^* = \frac{\alpha^2 \left((1 + \alpha^2)^2 |V_n^{r^*}| |V_n^{l^*}| - \alpha^2 (|V_n^{r^*}| + |V_n^{l^*}|)^2 \right)}{g(1 + \alpha^2)(\alpha^2 - 1)^2}, \quad (6.28)$$

$$E^{r^*} = \frac{\alpha^2 \left((\alpha^4 + \alpha^2 - 1)(V_n^{r^*})^2 + \alpha^2 (V_n^{l^*})^2 - 2|V_n^{r^*}| |V_n^{l^*}| \right)}{2(\alpha^2 - 1)(1 + \alpha^2)^2},$$

$$E^{l^*} = \frac{\alpha^2 \left((\alpha^4 + \alpha^2 - 1)(V_n^{l^*})^2 + \alpha^2 (V_n^{r^*})^2 - 2|V_n^{r^*}| |V_n^{l^*}| \right)}{2(\alpha^2 - 1)(1 + \alpha^2)^2}. \quad (6.29)$$

If the energy levels denote the two parameters of the period-two solution, (6.29) must be inverted to find the normal velocities that can be replaced in the solution equations.

The flight times are derived from (6.5):

$$\Delta t^{r^*} = \frac{2\alpha^2 (\alpha^2 |V_n^{r^*}| - |V_n^{l^*}|)}{g(\alpha^4 - 1)}, \quad (6.30)$$

$$\Delta t^{l^*} = \frac{2\alpha^2 (\alpha^2 |V_n^{l^*}| - |V_n^{r^*}|)}{g(\alpha^4 - 1)}.$$

These relationships correspond to the period-one solution ((6.10), (6.11) and (6.12)) if $E^{r^*} = E^{l^*}$ ($|V_n^{r^*}| = |V_n^{l^*}|$).

An elastic wedge can be simulated from non-elastic edges by adding $(1 - e)/(1 + e)|V_n^-|[k + 1]$ to the edges velocity.

Proposition 4 *Period-two orbits exist in the unactuated elastic wedge-billiard only for $\theta = 45^\circ$. They are uniquely defined by their energy level E^* and their impact radial velocity V_r and are unstable. For every $\theta \in (0^\circ, 90^\circ)$ and for every pair (E^{r^*}, E^{l^*}) , the actuated elastic wedge-billiard possesses a unique period-two orbit determined by the fixed point of $\mathcal{B}^2 = \mathcal{B} \circ \mathcal{B}$ (6.3). If $\theta < 45^\circ$, this orbit is either marginally stable or exponentially unstable, depending on the energy difference $E^{r^*} - E^{l^*}$. It is unstable if $\theta = 45^\circ$ and exponentially unstable if $\theta > 45^\circ$.*

Proof First, we derive the period-two orbits in the *square* wedge-billiard ($\theta = 45^\circ$, $\alpha = 1$) because several equations previously derived become singular. In this case, (6.21), (6.25) and (6.26) force the normal velocities to be equal:

$$|V_n^{r^*}| = |V_n^{l^*}| = |V_n^*| = |V_n^{-r^*}| = |V_n^{-l^*}| \quad (6.31)$$

so that each trajectory has the same energy: $E^{r^*} = E^{l^*} = E^*$. The second parameter of the period-two orbit is the radial velocity V_r^* since (6.27) is undetermined when $\alpha = 1$.

The period-two solution of the square wedge-billiard is then derived from (6.4), (6.2) and (6.5) with $\alpha = 1$:

$$|V_n^*| = \sqrt{2E^*}, \quad (6.32)$$

$$R^* = \frac{1}{2g} (2E^* - (V_r^*)^2), \quad (6.33)$$

$$\Delta t^{r^*}, \Delta t^{l^*} = \frac{\sqrt{2E^*} \pm |V_r^*|}{g}. \quad (6.34)$$

From (6.24), we have:

$$\dot{S}^{r^*} = -\dot{S}^{l^*} = \frac{|V_n^{r^*}| - |V_n^{l^*}|}{2}. \quad (6.35)$$

The steady-state edges velocities \dot{S}^{r^*} and \dot{S}^{l^*} are therefore equal to zero only if $|V_n^{r^*}| = |V_n^{l^*}|$, i.e. in the square configuration. Period-two orbits exist in the *unactuated* elastic wedge-billiard only in that configuration. Period-two orbits exist with any other wedge angle but require an actuation of the edges, according to (6.35).

Stability of these orbits is studied via the linearization of $\mathcal{B}^2 = \mathcal{B} \circ \mathcal{B}$ (with \mathcal{B} given in(6.3)) around its fixed point. We find the following jacobian matrix:

$$\begin{aligned} \left(\begin{array}{c} \delta V_r[k+2] \\ \delta |V_n|[k+2] \\ \frac{g}{\sqrt{|V_n^{r^*}||V_n^{l^*}|}} \delta R[k+2] \end{array} \right) &= \mathcal{M}_2 \left(\begin{array}{c} \delta V_r[k+1] \\ \delta |V_n|[k+1] \\ \frac{g}{\sqrt{|V_n^{r^*}||V_n^{l^*}|}} \delta R[k+1] \end{array} \right) \\ &= \mathcal{M}_2 \mathcal{M}_1 \left(\begin{array}{c} \delta V_r[k] \\ \delta |V_n|[k] \\ \frac{g}{\sqrt{|V_n^{r^*}||V_n^{l^*}|}} \delta R[k] \end{array} \right) \end{aligned} \quad (6.36)$$

with

$$\mathcal{M}_i = \left(\begin{array}{ccc} \frac{1-4\alpha^2-\alpha^4+4\alpha^2\chi_i}{(1+\alpha^2)^2} & \frac{2\alpha^2(1+\tau_i)}{(1+\alpha^2)^2} & \frac{-2\sqrt{\tau_i}}{1+\alpha^2} \\ \frac{\alpha^4+1-2\alpha^2}{2(\alpha^2-1)(1+\alpha^2)^2} & \frac{\alpha^4+1-2\alpha^2}{(1+\alpha^2)^2} & \frac{2}{(1+\alpha^2)\sqrt{\tau_i}} \\ \frac{2\alpha^2(1-\alpha^2+(1+\alpha^2)\chi_i+2\alpha^2\chi_i^2)}{(1+\alpha^2)^2\sqrt{\tau_i}} & \frac{2\alpha^4(1+\tau_i)(1+\chi_i)}{(1+\alpha^2)^2\sqrt{\tau_i}} & \frac{1-\alpha^2-2\alpha^2\chi_i}{1+\alpha^2} \end{array} \right)$$

and $\chi_i = (1 - \tau_i)/(1 - \alpha^2)$ for $i = 1, 2$. The parameter $\tau_1 = |V_n^{r^*}|/|V_n^{l^*}| = 1/\tau_2$ denotes the normal velocity ratio. These parameters capture the energy difference between both parabolas and have been defined as such only for computational convenience.

The eigenvalues of (6.36) were numerically computed, depending on α and τ_1 . Fig. 6.3 depicts the stability regions of the period-two solution in the parameter space (θ, τ_1) . As in the period-one stability analysis, one of the eigenvalues is always equal to 1, the energy being conserved over two impacts in the period-two orbit. The

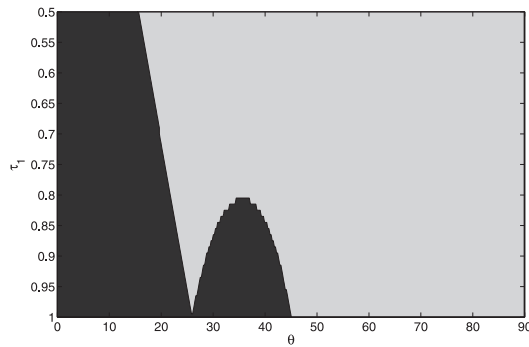


Figure 6.3: Stability regions of the period-two solution: marginal stability (black) and exponential instability (grey).

two remaining eigenvalues either are complex and lie on the unitary circle (black zone, marginal stability) or are real, at least one of them being outside the unitary circle (grey zone, instability).

Similarly to what was observed for the period-one orbit², Fig. 6.3 shows that all period-two orbits are exponentially unstable for $\theta > 45^\circ$. In contrast, marginally stable orbits coexist with unstable orbits for $\theta < 45^\circ$, depending on the energy difference $|E^{r^*} - E^{l^*}|$ via the ratio τ_1 . Finally, for $\theta = 45^\circ$, $|V_n^{r^*}| = |V_n^{l^*}|$ induces $\tau_1 = \tau_2 = 1$. The three eigenvalues of $\mathcal{M}_2\mathcal{M}_1$ are equal to 1. Because the dynamics become linear (see Sepulchre and Gerard, 2003), then the period-two orbits are unstable. \square

It is of interest to observe the unstable behavior of all period-two orbits for a particular value of θ about 26° . This value corresponds to $(1 - \alpha^2)/(1 + \alpha^2)^2 = 0.5$ (i.e. $\alpha = \sqrt{\sqrt{5} - 2}$), in which case two eigenvalues of the linearized system (6.13) are equal to $\pm i$. The linearized system (6.36) corresponds to a double iteration of (6.13) when $\tau_1 = 1$, resulting in two eigenvalues equal to $(\pm i)^2 = -1$. They split into two real eigenvalues, one of them outside the unit circle, when $\tau_1 \neq 1$. The same critical value of θ causes *uncontrollability* of a linearized model of the elastic wedge-billiard which is controlled with one edge. For this particular aperture, the dynamics of the normal velocity, the radial velocity and the energy decouple. At first order, the control input leaves each of these dynamics invariant (Gerard and Sepulchre, 2004).

²Note that the period-one eigenvalues (6.14) lie on a “slice” of Fig. 6.3, for $\tau_1 = \tau_2 = 1$ ($\chi_1 = \chi_2 = 0$). In that case, \mathcal{M}_1 and \mathcal{M}_2 are equal to (6.13).

6.4 Periodic orbits of the sinusoidally actuated wedge-billiard

None of the periodic orbits studied in Section 6.3 are attractors: either the linearized system is marginally stable or unstable. In this section, we introduce how a simple periodic actuation of the wedge can *isolate* and *stabilize* one of the periodic orbits, characterized by its energy level(s) (E^* for a period-one orbit or E^{r^*} and E^{l^*} for a period-two orbit).

The stabilization method presented in this section is completely similar to the one studied by Holmes (1982) in the bouncing ball dynamics (see Section 3.2.2), i.e. a sinusoidal actuation of the edges (3.7). Such an harmonic motion is the closest imitation of the fundamental cyclic motion of the juggler's hands. Moreover, we assume that this edges remain synchronized in anti-phase (in intrinsic space), such that their aperture remains constant throughout the cycles.

As previously mentioned, the special configuration of the square wedge-billiard turns out to bridge the bouncing ball dynamics studied in Section 3.2 and the wedge dynamics.

6.4.1 The square wedge-billiard

The steady-state velocity-energy relation of the square wedge-billiard (6.32) has exactly the same form as for a bouncing ball³, emphasizing the decoupling of the square wedge: the dynamics along each edge can be viewed as a 1 DOF independent bouncing ball motion that is unaffected by the bounces on the other axis (Sepulchre and Gerard, 2003), see Chapter 5 (Fig. 5.4). The parameter V_r^* determines the phase shift between the two bouncing balls.

The steady-state regime is characterized by two frequency-locking relations between the ball and the wedge (Ronsse et al., 2004):

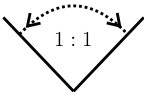
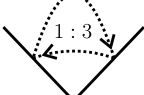
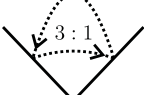


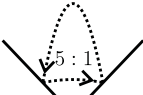
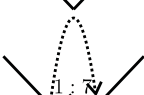
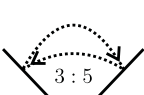
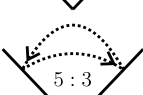
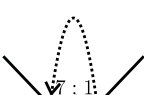
$$(t[k+2] - t[k])^* \equiv \Delta t^{r^*} + \Delta t^{l^*} = n \frac{2\pi}{\omega}, \quad (6.37)$$

$$(t[k+1] - t[k])^* \equiv \Delta t^{r^*} = (2m-1) \frac{\pi}{\omega} \quad (6.38)$$

where $(\bullet)^*$ denotes the steady-state solutions. These relations rest on the trivial assumption $m \leq n$, with m and $n \in \mathbb{N}$. Eq. (6.37) expresses that the ball period is a multiple of the edge vibration period: this is the frequency-locking relation of each dynamics similar to (3.10). Eq. (6.38) expresses that the phase difference between two successive impacts must be equal to an odd multiple of the vibration half-frequency. As a convention, m will be associated with the flight time between the right edge and the left edge: $\Delta t^{r^*} = (2m-1)\pi/\omega$, while the flight time between

³Consider simply that the bouncing ball dynamics refer to an exchange of a maximal *potential* energy E^* (at the top-point) and a maximal *kinetic* energy $\propto (V_n^*)^2$ (just before impacts), i.e. $|V_n^*| \propto \sqrt{E^*}$.

Table 6.1: Periodic orbits for the square wedge-billiard. $(x : y)$ denotes the ratio between both flight times where x (y) is associated to the flight from left to right (from right to left).

	m=1	m=2	m=3	m=4	...
n=1		X	X	X	
n=2			X	X	
n=3				X	...
n=4					
⋮			⋮		

the left edge and the right edge will be $\Delta t^{l*} = (2n - 2m + 1)\pi/\omega$ in the steady-state regime. Table 6.1 illustrates the first periodic orbits for the vibrating square wedge-billiard and the ratios between the low toss and the high toss flight times for each of these orbits. A sustained steady-state shower pattern will be characterized exactly by the same ratios, n denoting also the number of juggled balls. It is interesting to point out how the symmetry of the square wedge-billiard captures the symmetry of the juggler behavior. Beek and Lewbel (1995) wrote a very accessible paper on the “scientific aspects of juggling” where they present a compact notation for juggling patterns: *Site-swap* notation represents the order in which props are thrown and caught in each cycle of the juggle, assuming throws happen on beats that are *equally spaced in time*, being the case both in most of the common juggling patterns, and in the square wedge-billiard. The site-swap notation of the 3 balls shower is simply ‘51’, where the 5 refers to the duration of the high toss and the 1 to the time needed to pass the ball from one hand to the other on the lower part of the arc. Each $(x : y)$ orbit presented in Table 6.1 will then be “site-swap” noted ‘ xy ’.

Injecting the flight time solutions (6.34) in (6.37) and (6.38), we obtain the steady-state velocities of the periodic orbits of the square wedge-billiard, while the

energy E^* , the impact position R^* derive from (6.32) and (6.33):

$$E^* = \frac{(n\pi g)^2}{2\omega^2}, \quad (6.39)$$

$$|V_n^*| = \frac{n\pi g}{\omega}, \quad (6.40)$$

$$V_r^{r^*} = -\frac{(n-2m+1)\pi g}{\omega} = -V_r^{l^*}, \quad (6.41)$$

$$R^* = \frac{g}{2} \left(\frac{\pi}{\omega}\right)^2 (2m-1)(2n-2m+1). \quad (6.42)$$

The steady-state energy is independent of m . The radial velocity naturally corresponds to the period-one solution ($V_r^* = 0$) when $n = 2m - 1$ (see Table 6.1).

By considering the cartoon model introduced in Chapter 5 and a sinusoidal actuation along the axis perpendicular to the edges (see Fig. 5.4), the normal velocity is updated as: $V_n[k+2] = eV_n[k] + (1+e)\dot{S}[k+2]$, exhibiting the decoupling between the dynamics along each edge. The stability properties of the periodic orbits are immediately inherited from the decoupled dynamics, i.e. from the stability properties of the bouncing ball, assuming the small amplitude assumption⁴. Under this assumption, the parametric stability region is slightly different of (3.17) (Holmes, 1982):

$$n\pi \frac{1-e}{1+e} < \frac{\sqrt{2}A\omega^2}{g} < \sqrt{n^2\pi^2 \left(\frac{1-e}{1+e}\right)^2 + 1}. \quad (6.43)$$

Note that only $g/\sqrt{2}$ of the gravity field applies along each axis. The differences between the parametric stability regions characterized by (3.17) and (6.43) have been studied by Bapat et al. (1986). Significant differences between the exact and the approximated model are more likely if e is below about 0.8; nevertheless, the approximated model provides a good description of the qualitative dynamical behavior.

Consequently, each periodic orbit depicted in Table 6.1 is composed of two phase-locked period-one bouncing balls. They are stable if (6.43) is respected.

6.4.2 The general vibrating wedge-billiard

The dynamics of a ball in the general wedge-billiard do not decouple in two independent dynamics along each edge. The frequency-locking relation (6.37) between two successive impacts times on the same edge is still valid. In contrast, we introduce a scaling parameter ρ in (6.38) to take the energy dissymmetry into account:

$$\Delta t^{r^*} = (2m-1)\rho \frac{\pi}{\omega}. \quad (6.44)$$

⁴The small amplitude assumption of the bouncing ball assumes that the edges motion is much smaller than the ball motion, the impacts therefore occurring at a constant position, i.e. $s[k]$ constant $\forall k$.

The parameter ρ must fulfill $0 < \rho < \frac{2n}{2m-1}$, tuning the flight time Δt^{r^*} between 0 and $(t[k+2] - t[k])^*$.

Injecting the flight time solutions (6.30) in (6.37), we obtain a relation about the mean of the normal velocities:

$$|V_n^{r^*}| + |V_n^{l^*}| = \frac{\pi n g}{\omega} \frac{1 + \alpha^2}{\alpha^2} \quad (6.45)$$

that must be combined with (6.44) to obtain the steady-state normal velocities of the periodic orbits, while the energy levels, the radial velocities and the impact position derive from (6.27), (6.28) and (6.29):

$$E^{r^*} = \frac{1}{2\alpha^2} \left(\frac{n\pi g}{\omega} \right)^2 \left(\left(\frac{(2m-1)\rho}{2n} \right)^2 (\alpha^2 - 1) + 1 \right), \quad (6.46)$$

$$E^{l^*} = \frac{1}{2\alpha^2} \left(\frac{n\pi g}{\omega} \right)^2 \left(\left(\frac{2n - (2m-1)\rho}{2n} \right)^2 (\alpha^2 - 1) + 1 \right), \quad (6.47)$$

$$|V_n^{r^*}| = \frac{n\pi g}{\omega} \frac{(\alpha^2 - 1) \frac{(2m-1)\rho}{2n} + 1}{\alpha^2}, \quad (6.48)$$

$$|V_n^{l^*}| = \frac{n\pi g}{\omega} \frac{(1 - \alpha^2) \frac{(2m-1)\rho}{2n} + \alpha^2}{\alpha^2}, \quad (6.49)$$

$$V_r^{r^*} = \frac{-\pi g}{\omega} (n - (2m-1)\rho) = -V_r^{l^*}, \quad (6.50)$$

$$R^* = \frac{g(1 + \alpha^2)}{4\alpha^2} \left(\frac{\pi}{\omega} \right)^2 (2m-1)\rho(2n - (2m-1)\rho). \quad (6.51)$$

The energy exchange between the ball and the edges at each impact is:

$$\pm(E^{l^*} - E^{r^*}) = \pm \frac{\alpha^2 - 1}{2\alpha^2} \left(\frac{n\pi g}{\omega} \right)^2 \left(\frac{n - (2m-1)\rho}{n} \right).$$

In the bouncing ball dynamics, the bifurcation parameter is a non-dimensional amplitude proportional to the vibration amplitude A and to the square of the vibration frequency ω^2 (Holmes, 1982; Schaal et al., 1996). Therefore both these parameters can be used to generate the cascade of bifurcations. This non-dimensional parameter depends on ρ . This rests on a trigonometric relation between the steady-state edges phases at impact deriving from $\sin^2 \phi^{r^*} + \cos^2 \phi^{r^*} = 1$:

$$\cos^2 \phi^{r^*} + \cos^2 \phi^{l^*} - 2 \cos \phi^{r^*} \cos \phi^{l^*} \cos((2m-1)\rho\pi) = \sin^2((2m-1)\rho\pi) \quad (6.52)$$

which is not invertible.

Summarizing the derivations in this section, we obtain the following proposition:

Proposition 5 *The wedge-billiard model (6.3) with harmonic actuation $s(t) = A \sin(\omega t)$ isolates particular periodic orbits among those derived in Proposition 4.*

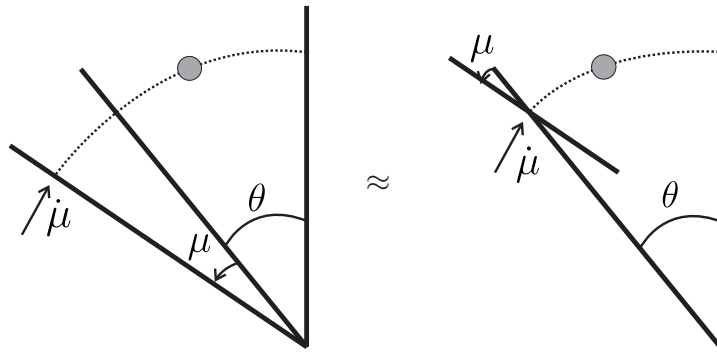


Figure 6.4: The controlled rotational wedge (left), and the simplified model when μ is small (right).

These orbits are characterized by (6.46) to (6.51) via n and m and satisfy frequency-locking relations between the ball and the edges ((6.37) and (6.44)). For the particular square wedge configuration ($\theta = 45^\circ$), (6.44) degenerates to (6.38). Considering a cartoon model for a sinusoidal actuation (the parallel actuation depicted in Fig. 5.4), the dynamics decouple into two 1 DOF dynamics along each edge. Stability of the isolated periodic orbits follows immediately from the bouncing ball stability (6.43).

6.5 Stabilization of periodic orbits by rotational actuation of the edges

The Wiper robot, presented in Section 6.6, uses rotational actuation of the edges instead of linear actuation as depicted in Fig. 5.4. A rotational implementation is indeed much simpler to design, since the arms can be directly actuated by DC motors. We examine in this section how rotational actuation modifies the model studied in the previous sections, both for period-one and period-two orbits.

With rotational actuation, the angle θ of each edge with the vertical is no longer constant, which significantly complicates the derivation of the flight map. To avoid the complication of computing that new flight map, a “small amplitude” assumption is introduced: we neglect the variation of θ in the derivation of the flight map but only take it into account in the derivation of the impact map. As illustrated in Fig. 6.4, this simplification amounts to assume that the impacts always occur at angle θ but that the angular actuation μ rotates the normal and *tangential* directions of the impacted edge by an angle μ (Fig. 6.4, right). This simplification neglects the displacement of the impact point and is more likely if $|\mu| \ll \theta$.

The Poincaré map of the rotational wedge is derived in Appendix 6.A of this chapter.

The general steady-state equations derived in Section 6.4 still hold in that case

(Eqs. (6.46) to (6.51)). The edges velocity being equal to $\dot{\mu}(t) = A\omega \cos(\omega t)$, the steady-state edges phases derive from (6.48), (6.49) and (6.60):

$$\begin{aligned}\phi^{r^*} &= \arccos \left(\frac{1-e}{1+e} \frac{n\pi g}{AR^*\omega^2} \frac{(\alpha^2-1)^{\frac{(1+e)\frac{(2m-1)\rho-e}{2n}}{1-e}} + 1}{\alpha} \right), \\ \phi^{l^*} &= \arccos \left(\frac{1-e}{1+e} \frac{n\pi g}{AR^*\omega^2} \frac{(\alpha^2-1)^{\frac{(1+e)\frac{(2m-1)\rho-1}{2n}}{1-e}} - 1}{\alpha} \right) - \pi.\end{aligned}\quad (6.53)$$

Because the steady-state impact position R^* is proportional to $1/\omega^2$ (6.51), the non-dimensional bifurcation parameter is now proportional to the vibration amplitude A only. The vibration frequency acts as a *temporal scaling factor* and does not influence the stability properties.

To analyze how the modified model affects the stability of periodic orbits, we numerically computed the eigenvalues of the linearized Poincaré map in two simple cases:

- The period-one orbits ($n = 2m - 1$, $\rho = 1$).
- The period-one and period-two orbits in the *square* rotational wedge ($\theta = 45^\circ$, $\rho = 1$).

6.5.1 Stability of period-one orbits

The simplest period-one orbit ($n = m = 1$) has been first mentioned as an open-loop stable orbit in a wedge-billiard with a rotational sinusoidal actuation by Schaal and Atkeson (1993). The stability region presented in this paper is in agreement with our results. This stability region has been obtained from a linearized model which does not rest on a “small amplitude” assumption. Accordance between stability regions obtained from both models is viewed as a validation of our “small amplitude” model.

The period-one orbits are particular cases of Equations (6.46) to (6.51) and Equation (6.53) with $n = 2m - 1$ and $\rho = 1$, which is required for period-one. We find:

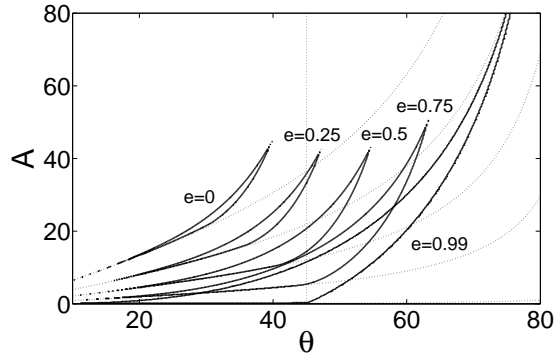
$$E^* = \frac{3 + \alpha^2}{8\alpha^2} \left(\frac{(2m-1)\pi g}{\omega} \right)^2, \quad (6.54)$$

$$|V_n^*| = \frac{1 + \alpha^2}{\alpha^2} \frac{(2m-1)\pi g}{2\omega}, \quad (6.55)$$

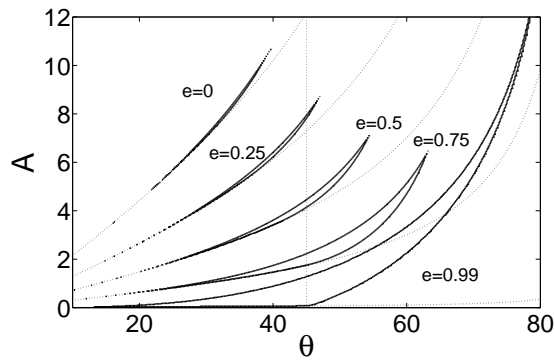
$$V_r^* = 0, \quad (6.56)$$

$$R^* = \frac{1 + \alpha^2}{4\alpha^2} \left(\frac{(2m-1)\pi}{\omega} \right)^2 g, \quad (6.57)$$

$$\phi^* = \arccos \left(\frac{1-e}{1+e} \frac{2\alpha}{A} \frac{1}{(2m-1)\pi} \right). \quad (6.58)$$



(a) $n = 1, m = 1$



(b) $n = 3, m = 2$

Figure 6.5: Parametric stability region of two period-one orbits in the general wedge (solid lines). The dotted lines denote the physical minimum value for the amplitude A (the arccos argument in (6.58) must be ≤ 1).

The stability is studied via the linearized Poincaré map of $\tilde{\mathcal{B}}$ (6.60) and of the flight time (6.5) around the period-one solution just derived. We find the Jacobian matrix (6.63) derived in Appendix 6.B of this chapter. Its eigenvalues were numerically computed for several values of e and α . Fig. 6.5 depicts the stability region for the first two period-one orbits ($n = 1, m = 1$ (a) and $n = 3, m = 2$ (b)). The superposed curves stand for different values of e .

A decreasing coefficient of restitution reduces the stability regions and shifts it in a zone corresponding to closer angles between the edges. We can see that even for $e = 0$, the first period-one orbit is still theoretically stabilizable with a sinusoidal vibration of the edges if the impacts occur with $\theta \in [15^\circ, 40^\circ]$.

We conclude that sinusoidal actuation of edges stabilizes period-one orbits, for any coefficient of restitution $e < 1$ and for a broad domain of wedge geometry. For $\theta > 45^\circ$ this exponential stability is in sharp contrast with the instability of the same periodic orbit in the fixed elastic wedge.

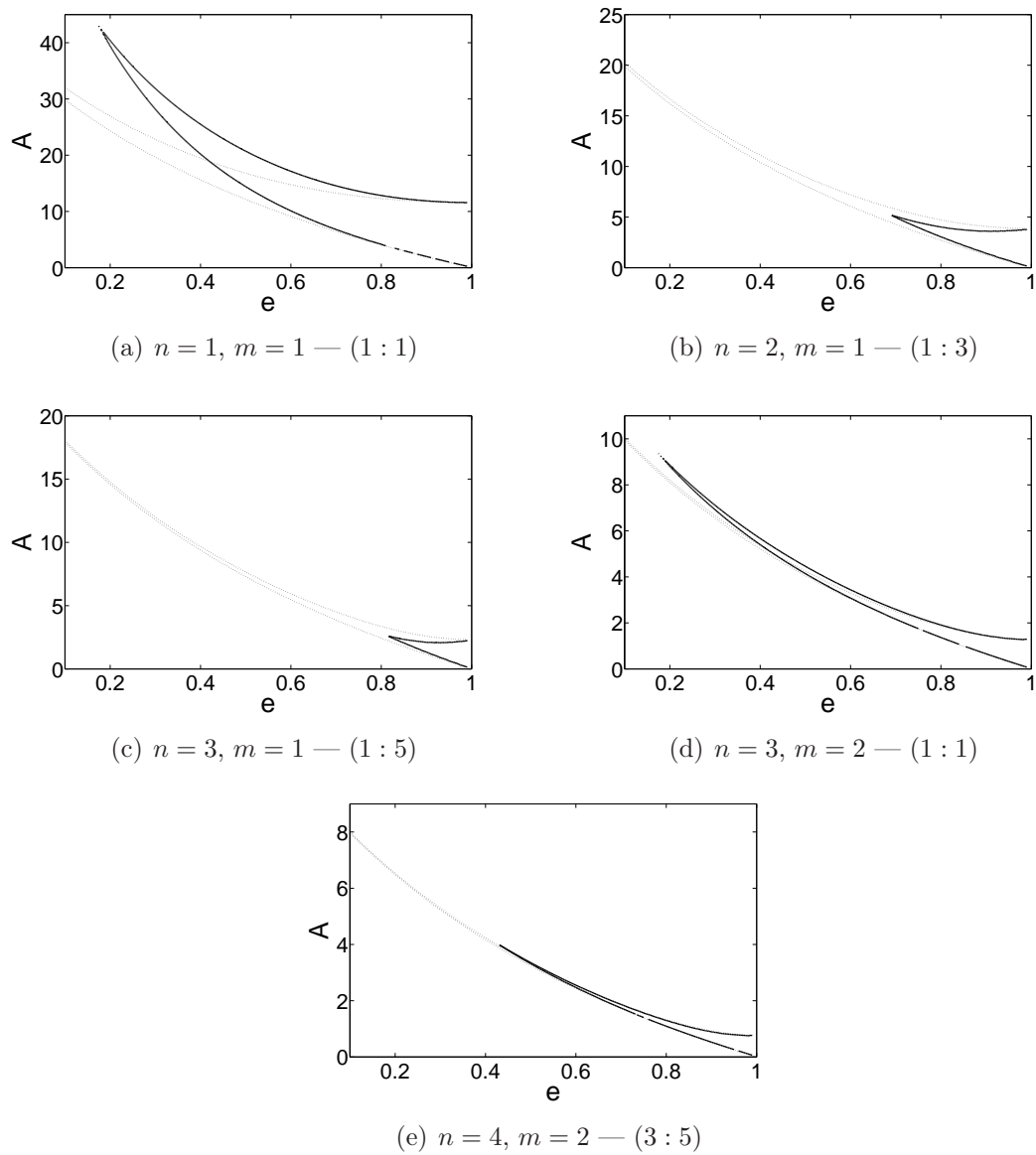


Figure 6.6: Parametric stability region of periodic orbits in the square wedge with linear actuation (dotted) and rotational actuation (solid).

6.5.2 Stability of period-two orbits in the square wedge

With *linear* actuation of the edges, we have shown in Section 6.4.1 that stability of period-two orbits in the square wedge follows from the bouncing ball dynamics analysis, yielding exponentially stable orbits in the parameter range (6.43). We now show that this stabilization result also holds with *rotational* actuation of the edges, by computing the eigenvalues of the Jacobian linearization of the map $\tilde{\mathcal{B}} \circ \tilde{\mathcal{B}} = \tilde{\mathcal{B}}^2$ (6.60) and of (6.5) around the period-two solution. We find the matrix $\tilde{\mathcal{M}}_2 \tilde{\mathcal{M}}_1$ derived in Appendix 6.B of this chapter (6.66).

Despite the new dynamics of the rotational wedge, there still exists a region in the parameters space where the absolute values of the four eigenvalues of this matrix are less than 1. This region is depicted on Fig. 6.6 (solid lines) for five of the periodic solutions emphasized: $(n = 1, m = 1)$ and $(n = 3, m = 2)$ are two $(1 : 1)$ period-one solutions depicted in 6.6(a) and 6.6(d), respectively; while $(n = 2, m = 1 - (1 : 3))$, $(n = 3, m = 1 - (1 : 5))$ and $(n = 4, m = 2 - (3 : 5))$ are three period-two solutions depicted in 6.6(b), 6.6(c) and 6.6(e), respectively. Each of those stability regions is compared with the corresponding stability region of the double bouncing balls system (dotted lines), where $\sqrt{2}A$ has been replaced by AR^* in (6.43). These stability regions clearly overlap more accurately for a high coefficient of restitution e . This makes a physical sense: the largest the coefficient of restitution, the smallest the vibration, and thus the more acceptable the small angle assumption.

Note that each of the curves depicted in Fig. 6.5 crosses the $\theta = 45^\circ$ line (light dotted) with intervals corresponding to those drawn in Figs 6.6(a) and 6.6(d), for the corresponding values of e .

6.5.3 Stability of period-two orbits in the actuated non-square wedge

The eigenvalues of the Jacobian matrix of the period-two orbits in the non-square wedge have not been computed. By analogy with the period-one orbits, we expect the conclusions obtained for the square wedge to persist in a range of values around $\theta = 45^\circ$.

The results of this section are summarized in the following proposition:

Proposition 6 *For a broad range of parameters (θ, e, A) , a sinusoidal actuation of the edges around a common fixed point (i.e. rotational actuation) achieves exponential stability of isolated periodic orbits. In particular, Fig. 6.5 illustrates the parametric stability region of two period-one orbits; and Fig. 6.6 illustrates the parametric stability region of five periodic orbits in the square configuration.*

6.6 Experimental results

This section describes an experimental validation of the stability results derived in the previous section for period-one and period-two orbits⁵.

The experimental validations have been realized with the Wiper robot, described in Chapter 5 and pictured in Fig. 5.2. The goal of the crude model we derived in Sections 6.2 to 6.5 is to capture the main effect of sensorless actuation of Wiper. The good matching between our experimental data and the theoretical predictions (see the rest of this section) is the best argument we can provide to validate the model, at least for the period-one motion.

6.6.1 Stabilization of period-one orbits

Our first experimental result is the stabilization of the first period-one orbit ($n = m = 1$) with rotational sinusoidal actuation of the edges. According to Fig. 6.5(a), two parameters are supposed to be crucial in the determination of the theoretical stability region: α , which is a geometrical parameter of the wedge and is therefore derived from the edges position, and the coefficient of restitution e , which on the contrary is difficult to estimate.

For a set of initial wedge aperture, we isolated experimentally the amplitude domains where the first period-one motion is stable. The experiments were conducted with a table inclined at an angle of 15° and a vibration frequency tuned in order to have a steady-state impact position R^* close to 0.7m (Equation (6.57)). Both parameters serve as tempo scaling factors and do not influence the stability regions.

Fig. 6.7 exhibits the experimental results obtained: all the tested conditions are marked by a point. The white and light gray zones are simply crude “contour” interpolations of the observed stability regions: all experimentally stable conditions belong to the white set. The light gray set contains the conditions which have been sorted as fragile but stable in the sense that either the period-one was stable, but only for a limited number of impacts (basically more than 10 but less than 30), or the puck described a complex motion confined around the period-one solution. The dark gray zone covers the experimental instability region, and the black zone excludes the experimental conditions leading to a risk of collision between the edges or with the table frame.

In order to compare the experimental results with the theoretical predictions, we superposed the theoretical stability region (solid lines) on Fig. 6.7, for $e = 0.5$. This region fits very well the experimental results and therefore validates the model and the mathematical analysis presented in the previous sections.

We note that Fig. 6.7 and Fig. 6.5(a) should be compared with caution. In Fig. 6.7, the parameter along the horizontal axis is the mean edge angle which is easily determined experimentally. However, the mean edge angle differs from the impact

⁵The interested reader will find two movies illustrating the stabilization of these periodic orbits on <http://ieeexplore.ieee.org> (Ronsse et al., 2006) or on the first author’s homepage.

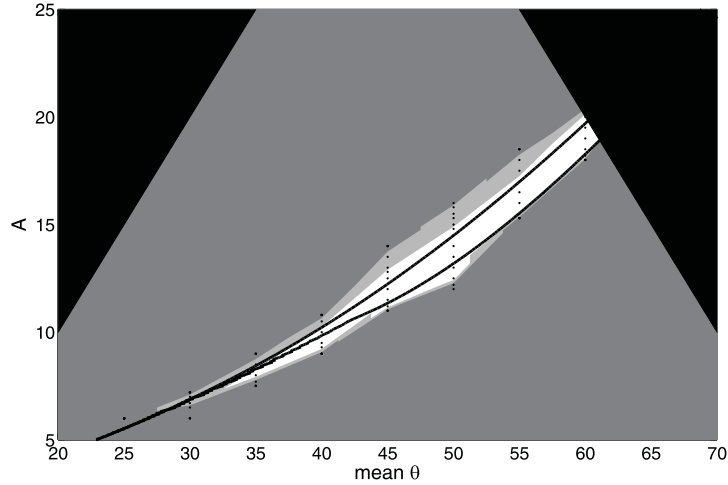


Figure 6.7: Experimental results on period-one stabilization: the points correspond to the tested conditions, the white zone surrounds the stability region, the light gray zone surrounds the “weak stability” region (see text), the dark gray zone depicts the instability region and the black zone excludes the non-secure zone. The results are compared with the theoretical prediction (solid lines) for $e = 0.5$.

angle, used as a parameter in Fig. 6.5. This explains why the theoretical parameter stability regions in Fig. 6.7 appears to be shifted and elongated compared to the corresponding region in Fig. 6.5(a).

6.6.2 Stabilization of period-two orbits

Experimental stabilization of period-two orbits turned out to be much more challenging. This is partly explained by the reduced stability regions of period-two orbits (see Fig. 6.6), but we also point out two additional reasons supporting that fact:

- The *basins of attraction* of the period-two orbits are much smaller than the period-one ones: a period-two orbit will be stabilized with a faster vibration frequency than a period-one orbit with an equivalent steady-state impact position (compare the ω obtained from Equations (6.51) and (6.57) for similar values of R^*). The period-two orbits are therefore more sensitive to the *phase* initial condition.
- The nonzero tangential impact velocity in period-two orbits causes the puck to *spin*. This phenomenon, not captured by the model, likely affects the stability properties and requires further investigations. See Spong (2001) for a study on the control of the spin dynamics.

We focused on the stabilization of the first period-two orbit ($n = 2, m = 1$). Fig. 6.6(b) shows that this periodic solution is not stable in the square configuration for

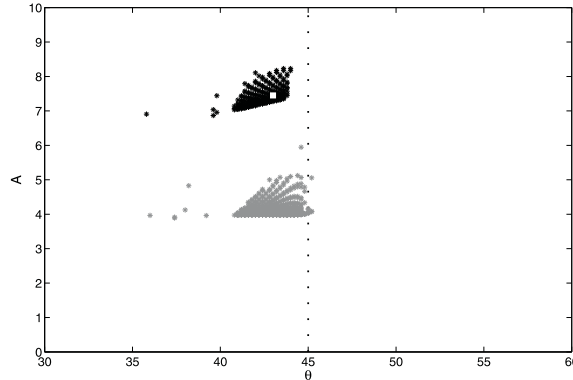


Figure 6.8: Stability region of the $(n = 2, m = 1)$ period-two orbit in the general Wiper for $e = 0.5$ (black points) and $e = 0.7$ (gray points).

the expected coefficient of restitution ($e \approx 0.5$). The Jacobian matrix of the period-two orbits in the general Wiper being hard to calculate, we preferred to simulate numerically the effect of small perturbations in our dynamical model, around the period-two limit cycle.

The points lying on Fig. 6.8 correspond to parameters values where a small perturbation of the period-two solution decreases through the impacts. These points therefore give an idea of the parametric stability region of that period-two orbit. Fig. 6.8 is consistent with Fig. 6.6(b)⁶: the parametric stability region has no intersection with the 45° black dotted line for e smaller than 0.7.

We successfully stabilized the period-two orbit in the lab during more than 50 impacts with a vibration amplitude A equal to 7.45° . The impact angular position has been visually estimated around 43° . This point is marked by a white square in Fig. 6.8 and clearly belongs to the numerically predicted stability region of the $(n = 2, m = 1)$ period-two orbit. This result opens the door to the stabilization of juggling patterns implying several pucks (two in this case), requiring only a temporal separation of the pucks equal to $2\pi/\omega$. In this way, Wiper would mimic the popular *shower* juggling pattern.

6.7 Conclusion

This chapter has established the experimental validation of the sensorless stabilization of bounce juggling patterns in the Wiper robot, described in Chapter 5. This result is also supported by a mathematical analysis of the modified stability prop-

⁶Let us recall that Figs 6.6(b) and 6.8 slice differently the stability region in the 3D parameter space (e, θ, A) : Fig. 6.6(b) slices the parameter space for $\theta = 45^\circ$ while Fig. 6.8 slices the parameter space for $e = 0.5$ and $e = 0.7$. These figures match at their intersections: $(\theta = 45^\circ, e = 0.5)$ and $(\theta = 45^\circ, e = 0.7)$.

erties: from periodic orbits which have been proved to be unstable, we derived an actuation law which stabilizes the same patterns.

Aiming at mimicking the popular *shower* juggling pattern, in Section 6.3 two particular periodic solutions of the wedge-billiard were studied: the period-two orbit, and its degenerate case, i.e. the period-one orbit. These periodic solutions have been proved to be either marginally stable or unstable for an uncontrolled elastic wedge-billiard. In Section 6.4, we derived the steady-state periodic orbits of a periodically actuated wedge-billiard. For the particular *square* wedge-billiard configuration, this generalizes the results on the bouncing ball dynamics (Holmes, 1982) to stabilize the wedge-billiard periodic orbits. A practical implementation of this stabilization requires a different configuration which has been modeled in Section 6.5. Within a single robot, several juggling patterns can therefore be stabilized through sensorless actuation, at least theoretically.

Finally, these theoretical predictions have been validated by several experimental results on *Wiper* robot, as explained in Section 6.6. Fig. 6.7 emphasized that our model under-estimated the stability region for the first period-one orbit. The dynamical properties that are not captured by our model seem to have a *stabilizing* effect on the period-one. Conversely, the period-two orbits were never stabilized during more than 30 seconds in our actual setup, while the model predicted reasonable parametric stability regions. We suppose that the *spin* effect, not captured in the map \mathcal{B} (6.60) while permanent in period-two trajectories, is highly destructive for stability; and that the sensorless control is not *robust* enough to cope with these unmodeled dynamics.

This chapter content has been published in Ronsse et al. (2006).

6.A Iteration map of the rotationally actuated wedge-billiard

Under the "small amplitude" assumption (Fig. 6.4), the impact rule \mathcal{I} captures the angular rotation. It is now given by

$$M(\mu[k]) \begin{pmatrix} V_r[k] \\ V_n[k] \end{pmatrix} = \begin{pmatrix} 1 & 0 \\ 0 & -e \end{pmatrix} M(\mu[k]) \begin{pmatrix} V_r^-[k] \\ V_n^-[k] \end{pmatrix} + \begin{pmatrix} 0 \\ \frac{1+e}{\alpha} R[k] \end{pmatrix} \dot{\mu}[k] \quad (6.59)$$

with $M(\mu)$ denoting the rotation matrix of the edge:

$$M(\mu) = \begin{pmatrix} \cos \mu & \alpha \sin \mu \\ -\frac{\sin \mu}{\alpha} & \cos \mu \end{pmatrix}$$

and $\mu[k] = \mu(t[k])$ ($\dot{\mu}[k] = \dot{\mu}(t[k])$) denoting the edge position (velocity) at impact time $t[k]$. The presence of $R[k]$ in (6.59) is due to a second important feature introduced by the rotational actuation: the energy exchange with the edges depends

now on the impact position $R[k]$. The map $\tilde{\mathcal{B}}$ of the rotational wedge is given by:

$$\begin{aligned} \begin{pmatrix} V_r[k+1] \\ V_n[k+1] \end{pmatrix} &= J(\mu[k+1]) \begin{pmatrix} |V_n|[k] - V_r[k] - |V_n^-|[k+1] \\ |V_n^-|[k+1] \cdot \text{sign}(V_n[k]) \end{pmatrix} \\ &\quad + \frac{1+e}{\alpha} \begin{pmatrix} -\alpha \sin \mu[k+1] R[k+1] \\ \cos \mu[k+1] R[k+1] \end{pmatrix} \dot{\mu}[k+1], \\ R[k+1] &= R[k] + \frac{1}{2g} V_r^2[k] + \frac{\alpha^2}{2g} V_n^2[k] \\ &\quad - \frac{1}{2g} (|V_n|[k] - V_r[k] - |V_n^-|[k+1])^2 - \frac{\alpha^2}{2g} |V_n^-|^2[k+1] \end{aligned} \quad (6.60)$$

with

$$J(\mu) = M(-\mu) \begin{pmatrix} 1 & 0 \\ 0 & -e \end{pmatrix} M(\mu) = \begin{pmatrix} \cos^2 \mu - e \sin^2 \mu & \frac{\alpha(1+e)}{2} \sin 2\mu \\ \frac{1+e}{2\alpha} \sin 2\mu & \sin^2 \mu - e \cos^2 \mu \end{pmatrix}. \quad (6.61)$$

The flight time is still given by (6.5).

The ‘‘small amplitude’’ assumption is done around the steady-state periodic orbits. They are therefore unchanged with respect to those which have been derived in Section 6.4. The actual actuation law is then:

$$\mu(t) = A (\sin \omega t - \sin (\{\phi^{r*}, \phi^{l*}\})), \quad (6.62)$$

providing $\mu^* = 0$.

6.B Jacobian matrices

The linearized Poincaré map of the period-one orbits of the rotational wedge-billiard is the matrix $\tilde{\mathcal{M}}$:

$$\begin{pmatrix} \frac{\omega}{g} \delta V_r[k+1] \\ \frac{\omega}{g} \delta |V_n|[k+1] \\ \frac{\omega^2}{\pi g} \delta R[k+1] \\ \omega t[k+1] \end{pmatrix} = \tilde{\mathcal{M}} \begin{pmatrix} \frac{\omega}{g} \delta V_r[k] \\ \frac{\omega}{g} \delta |V_n|[k] \\ \frac{\omega^2}{\pi g} \delta R[k] \\ \omega t[k] \end{pmatrix} \quad (6.63)$$

that is given by:

$$\tilde{\mathcal{M}} = \begin{pmatrix} \frac{1-4\alpha^2-\alpha^4}{(1+\alpha^2)^2} - 2\mu_{11} & \frac{4\alpha^2}{(1+\alpha^2)^2} - (\alpha^2-1)\mu_{11} & -\frac{4\alpha^2}{(2m-1)(1+\alpha^2)^2} - \frac{2}{(2m-1)}\mu_{11} & \frac{-1-e}{1+e} 2(1+\alpha^2) \\ \frac{2e(\alpha^2-1)}{(1+\alpha^2)^2} + (2m-1)\mu_{21} & \frac{e(\alpha^2-1)^2}{(1+\alpha^2)^2} + \mu_{22} & \frac{4e\alpha^2}{(2m-1)(1+\alpha^2)^2} + \mu_{21} & \frac{-(1-e)(1+\alpha^2)(2m-1)^2 \Gamma'}{4\alpha^3} \\ \frac{(2m-1)(1-\alpha^2)}{1+\alpha^2} & \frac{2(2m-1)\alpha^2}{1+\alpha^2} & \frac{1-\alpha^2}{1+\alpha^2} & 0 \\ \frac{4\alpha^2}{(1+\alpha^2)^2} & \frac{2\alpha^2(\alpha^2-1)}{(1+\alpha^2)^2} & \frac{4\alpha^2}{(2m-1)(1+\alpha^2)^2} & 1 \end{pmatrix} \quad (6.64)$$

with

$$\begin{aligned}\mu_{11} &= \frac{1-e}{1+e} \frac{4\alpha^2}{1+\alpha^2}, \\ \mu_{21} &= (1-e) \left(\frac{-(2m-1)\Gamma'}{\alpha(1+\alpha^2)} + \frac{2(1-\alpha^2)}{(2m-1)(1+\alpha^2)} \right), \\ \mu_{22} &= (1-e) \left(\frac{(1-\alpha^2)(2m-1)^2\Gamma'}{2\alpha(1+\alpha^2)} + \frac{4\alpha^2}{1+\alpha^2} \right), \\ \Gamma' &= \sqrt{\left(\left(\frac{1+e}{1-e} \right) A\pi^2 \right)^2 - \left(\frac{2\pi\alpha}{2m-1} \right)^2}.\end{aligned}$$

Note that the determinant of $\tilde{\mathcal{M}}$ is equal to

$$|\tilde{\mathcal{M}}| = \frac{e((1-e)(3\alpha^2-1) + 2(1+\alpha^2))}{(1+e)(1+\alpha^2)} \quad (6.65)$$

which is equal to 1 in the elastic case ($e = 1$), $\forall \alpha$. This illustrates that the sinusoidal input does not achieve exponential stability of the period-one orbit in the *elastic* wedge, because all the eigenvalues of this matrix cannot be < 1 in that case.

The linearized Poincaré map of the periodic orbits of the rotational *square* wedgebilliard is the matrix $\tilde{\mathcal{M}}_2\tilde{\mathcal{M}}_1$:

$$\begin{aligned}\begin{pmatrix} \frac{\omega}{g}\delta V_r[k+2] \\ \frac{\omega}{g}\delta|V_n|[k+2] \\ \frac{\omega^2}{\pi g}\delta R[k+2] \\ \omega t[k+2] \end{pmatrix} &= \tilde{\mathcal{M}}_2 \begin{pmatrix} \frac{\omega}{g}\delta V_r[k+1] \\ \frac{\omega}{g}\delta|V_n|[k+1] \\ \frac{\omega^2}{\pi g}\delta R[k+1] \\ \omega t[k+1] \end{pmatrix} \\ &= \tilde{\mathcal{M}}_2\tilde{\mathcal{M}}_1 \begin{pmatrix} \frac{\omega}{g}\delta V_r[k] \\ \frac{\omega}{g}\delta|V_n|[k] \\ \frac{\omega^2}{\pi g}\delta R[k] \\ \omega t[k] \end{pmatrix},\end{aligned} \quad (6.66)$$

$\tilde{\mathcal{M}}_1$ being given by

$$\tilde{\mathcal{M}}_1 = \begin{pmatrix} -\frac{2\eta}{\eta+\nu} - \frac{1-e}{1+e} \frac{2(\eta+\nu)}{\nu} & 1 & -\frac{2}{\eta+\nu} - \frac{1-e}{1+e} \frac{2(\eta+\nu)}{\eta\nu} & -\frac{1-e}{1+e} \frac{(\eta+\nu)^2}{\eta\nu} \\ \frac{-e(\nu-\eta)}{\eta+\nu} + (1-e) \left(\frac{2\eta\beta}{\eta+\nu} + \frac{\nu-\eta}{\nu} \right) & (1-e) \frac{\eta+\nu}{\nu} & \frac{2e}{\eta+\nu} + (1-e) \left(\frac{2\beta}{\eta+\nu} + \frac{\nu-\eta}{\nu} \right) & (1-e)\beta \\ \frac{(\nu-\eta)\eta}{\eta+\nu} & \eta & \frac{\nu-\eta}{\eta+\nu} & 0 \\ \frac{2\eta}{\eta+\nu} & 0 & \frac{2}{\eta+\nu} & 1 \end{pmatrix} \quad (6.67)$$

with

$$\beta = \frac{(\nu+\eta)(\eta-\nu)}{\nu\eta} - \frac{\nu\eta}{2} \sqrt{\left(\left(\frac{1+e}{1-e} \right) A\pi^2 \right)^2 - \left(\frac{2n\pi}{(2m-1)(2n-2m+1)} \right)^2}.$$

In (6.67), $\eta = 2m - 1$ and $\nu = 2n - 2m + 1$ depends on the steady-state flight times. $\tilde{\mathcal{M}}_2$ has exactly the same structure as $\tilde{\mathcal{M}}_1$ with an exchange between ν and η .

Chapter 7

Rhythmic Feedback Control of Wiper in Blindness

Music and rhythm find their way
into the secret places of the soul.

Plato

7.1 Introduction

In Chapter 6, we provided experimental validation of a *sensorless* control law (a purely sinusoidal actuation of the juggler arms) that robustly stabilizes the period-one orbit (Fig. 6.2(a)), but failed to robustly stabilize the period-two orbit (Fig. 6.2(b)) for more than a few seconds. The aim of the present chapter is consequently to investigate whether adding feedback to the loop may help to robustly stabilize the period-two. The control law proposed in the present chapter can be interpreted as a phase and amplitude modulation of the sinusoidal control law, based on the feedback information provided by the impact times. The technical material of this hybrid control strategy (discrete feedback for continuous-time actuation) has been presented for the bouncing ball in Chapter 4.

In Section 7.2, we briefly generalize the bouncing ball strategy to the special configuration of Wiper that reduces to two coupled bouncing balls (see Section 5.2). Along each decoupled dynamics — i.e. each edge — the control algorithm is exactly similar to (4.15). Zero static error between the frequencies of these dynamics¹ is ensured through the integral control described in Section 4.3.3.

The more accurate model of Wiper, based on the wedge-billiard described in Section 6.2 and derived in Section 6.A, is considered in Section 7.3. Discrete feedback control based on impact times is realized in a similar manner to the bouncing ball control: a model-based *observer* is synchronized with the actual dynamics through

¹Such that the phase-lag between them is fixed and invariant.

the impact times. Sustained experimental stabilization of the period-two orbit is also provided. Once again, let us emphasize that our experimental validation suffers from large discrepancies between the wedge-billiard model and the real setup dynamics. For example, the Newton impact model does not capture the *spin* effect of the puck, clearly visible in the period-two pattern. However, the focus of our approach is precisely to validate the *robustness* of a model-based control scheme in a real setup in spite of the many discrepancies between the model and the experimental setup. The robustness has been quantified in Chapter 4 via the *acceleration* of the actuator at impact. Obviously, we tuned our controller to match with the optimal acceleration (4.21) locally around impacts, such that the closed-loop robustness there obtained is large enough to compensate for the model discrepancies.

7.2 Feedback Control of the Simplified Wedge-Billiard

First, let us generalize the robust feedback control strategy discussed for the bouncing ball (Chapter 4) to the special configuration of the wedge-billiard, presented in Section 5.2 and pictured in Fig. 5.4. The two edges are then assumed to remain aligned with the two orthogonal axes of a fixed reference frame (this requires parallel actuation of the edges, in contrast with the rotational actuation of the Wiper robot, see Chapter 5). In this special configuration, the resulting dynamics nicely decouple: the dynamics along each axis are the dynamics of a one-dimensional bouncing ball (see Section 5.2 and Sepulchre and Gerard, 2003).

A period-two orbit of the planar juggler projects onto a period-one orbit along each axis (see Fig. 5.4). The phase shift Φ^* (not represented in the figure) between the x -orbit and the y -orbit controls the shape (that is the apex difference between the low toss and the high toss) of the period-two planar orbit, since the impact times obey:

$$\begin{aligned} t[k_x] &= \frac{2\pi k_x}{\omega}, \\ t[k_y] &= \frac{2\pi k_y + \Phi^*}{\omega} \end{aligned} \tag{7.1}$$

where k_x and k_y denote the k^{th} impact along the x and y axes, respectively; and ω still denotes the cycle frequency.

Based upon this analogy, the stabilization of the period-two planar orbit of the juggler reduces to the stabilization of a period-one orbit in two independent 1D bouncing balls. As a consequence, the blind feedback control — i.e. based only on impact *times* measurement — introduced in Chapter 4 directly applies for the simplified wedge billiard. Any period-one or period-two orbit can be stabilized through proper control of the *phase* between the two decoupled dynamics. Phase

control with no static error can be achieved with the integral control described in Section 4.3.3.

7.3 Experimental Validation with the Wiper Robot

7.3.1 Experimental setup

In the *Wiper* robot, both edges are actuated around their fixed point, like in the general wedge-billiard model (see Sections 6.2 and 6.A, and Fig. 6.1). Fig. 5.2 is a picture of *Wiper*.

The actuated metallic edges are controlled by two independent motors, which are mounted close to each other (about 10cm) since the model assumes that both edges rotate around the same point. Both motors are controlled with a real-time computer running with XPCTARGET (THE MATHWORKS[®]). Impact times are detected by two accelerometers mounted at the top of the edges to record the high-frequency vibrations generated by the impacts. More technical details can be found in Appendix B.1.

7.3.2 From the bouncing ball model to the wiper model

The double bouncing ball model presented in Section 7.2 is obviously a crude model of the Wiper robot: it neglects the coupling resulting from a rotational actuation of the edges, and a steady-state aperture possibly different from $2\theta = 90^\circ$. However, a more accurate model of Wiper was derived in Chapter 6², under the small angle assumption (Fig. 6.4). Despite this assumption, the model predicted a parametric stability region of the period-one orbit which is in excellent agreement with experiments (Fig. 6.7).

The Wiper model (see 6.60) has three state variables — V_r , V_n and R — and two input variables — $\mu[k]$ and $\dot{\mu}[k]$, denoting the impacted edge position w.r.t. θ (left) or $-\theta$ (right), and velocity at impact k — see Figure 6.1. Injecting the flight time (6.5) into the state-space model (6.60) gives the following state-space model, depending explicitly on the time difference:

$$\begin{aligned} \begin{pmatrix} V_r[k+1] \\ V_n[k+1] \end{pmatrix} &= J(\mu[k+1]) \begin{pmatrix} \frac{1-\alpha^2}{1+\alpha^2} V_r[k] + \frac{2\alpha^2}{1+\alpha^2} |V_n|[k] - g(t[k+1] - t[k]) \\ \left(\frac{-2}{1+\alpha^2} V_r[k] + \frac{1-\alpha^2}{1+\alpha^2} |V_n|[k] + g(t[k+1] - t[k]) \right) \text{sign}(V_n[k]) \end{pmatrix} \\ &\quad + \frac{1+e}{\alpha} \begin{pmatrix} -\alpha \sin \mu[k+1] R[k+1] \\ \cos \mu[k+1] R[k+1] \end{pmatrix} \dot{\mu}[k+1], \quad (7.2) \\ R[k+1] &= \frac{1+\alpha^2}{4g} (V_n^2[k] - (|V_n|[k] - g(t[k+1] - t[k]))^2) \end{aligned}$$

with the rotation matrix $J(\mu)$ given by (6.61).

²See also Lehtihet and Miller (1986); Sepulchre and Gerard (2003); Gerard and Sepulchre (2004, 2005); Chang et al. (2005); Ronsse et al. (2005, 2006)

The output control law (4.15) derived in Chapter 4 for the bouncing ball is adapted for Wiper as follows:

- (i) **State observer:** The deadbeat velocity observer (4.14) is replaced by a copy of Wiper's dynamics (7.2), in which we substitute estimated variables \hat{V}_r , \hat{V}_n , \hat{R} to the state variables V_r , V_n , R ; and where the measured flight time is injected from the measurements (see (6.5)) to synchronize the observer with the actual state variables:

$$\begin{aligned} \begin{pmatrix} \hat{V}_r[k] \\ \hat{V}_n[k] \end{pmatrix} &= J(\mu[k]) \begin{pmatrix} \frac{1-\alpha^2}{1+\alpha^2} \hat{V}_r[k-1] + \frac{2\alpha^2}{1+\alpha^2} |\hat{V}_n|[k-1] - g(t[k] - t[k-1]) \\ \left(\frac{-2}{1+\alpha^2} \hat{V}_r[k-1] + \frac{1-\alpha^2}{1+\alpha^2} |\hat{V}_n|[k-1] + g(t[k] - t[k-1]) \right) \text{sign}(\hat{V}_n[k-1]) \end{pmatrix} \\ &\quad + \frac{1+e}{\alpha} \begin{pmatrix} -\alpha \sin \mu[k] \\ \cos \mu[k] \end{pmatrix} \hat{R}[k] \dot{\mu}[k], \\ \hat{R}[k] &= \frac{1+\alpha^2}{4g} \left(\hat{V}_n^2[k-1] - \left(|\hat{V}_n|[k-1] - g(t[k] - t[k-1]) \right)^2 \right). \end{aligned} \quad (7.3)$$

We suppose that the inputs $\mu[k]$ and $\dot{\mu}[k]$ are directly available from the measured trajectory of the edges $\mu(t)$ and the impact times. This observer displays excellent convergence properties in simulations.

- (ii) **Tracking controller:** The tracking controller (4.4), (4.5), (4.6) is adapted to the Wiper model. The desired next impact time is estimated on the basis of (6.5):

$$t_u[k+1] = t[k] + \frac{1}{g} \left(|\hat{V}_n^-|[k+1] + \frac{(\alpha^2 - 1)|\hat{V}_n|[k] + 2\hat{V}_r[k]}{1 + \alpha^2} \right). \quad (7.4)$$

The position reference is simply $\mu_\rho^* = 0$ since the objective is to stabilize periodic orbits of Wiper whose impacts occur at $\pm\theta$. The ‘‘local’’ velocity of the edge, at the impact point, depends obviously both on the velocity input $\dot{\mu}_\rho[k+1]$ and the impact radial position $R[k+1]$. Defining $\dot{S} = \dot{s}/\sin\theta$, where \dot{s} is equal to this local velocity, one has therefore $\dot{\mu}[k+1] = \alpha\dot{S}[k+1]/R[k+1]$. This ‘‘local’’ edge velocity derives from the impact rule:

$$\dot{S}_u[k+1] = \frac{|V_n|_\rho[k+1] - e|\hat{V}_n^-|[k+1]}{1+e} \quad (7.5)$$

where the reference post-impact velocity $|V_n|_\rho[k+1]$ is equal to:

$$|V_n|_\rho[k+1] = \frac{g}{2\alpha^2} (t_\rho[k+3] - t_u[k+1]) - \frac{g(1-\alpha^2)}{2\alpha^2} (t_\rho[k+2] - t_u[k+1]) \quad (7.6)$$

and is computed from the impact times reference. In the square configuration ($\alpha = 1$), this equation becomes similar to (4.25). In that case, the wedgebilliard dynamics decouple into two bouncing ball dynamics, one along each edge, as mentioned in Sections 6.4 and 7.2.

Finally, the estimate of the radial position is obtained from the estimated state variables (see (6.60)):

$$\begin{aligned}
 R_u[k+1] &= \hat{R}[k] + \frac{1}{2g}\hat{V}_r^2[k] + \frac{\alpha^2}{2g}\hat{V}_n^2[k] \\
 &\quad - \frac{1}{2g}(|\hat{V}_n|[k] - \hat{V}_r[k] - |\hat{V}_n^-|[k+1])^2 - \frac{\alpha^2}{2g}(\hat{V}_n^-)^2[k+1].
 \end{aligned} \tag{7.7}$$

- (iii) **Continuous-time actuation:** The piecewise quadratic control law (4.7) generates obviously sharp position transients at impact, even in steady-state. In order to smoothen the actuation, we chose to design a closed-loop control that reaches the desired position and velocity at impact, but that is smooth in steady-state. This modification helped to prevent false impact detection and motor damages in real experiments. This was realized by adapting the open-loop sinusoidal law (3.7) to take feedback into account, for amplitude and phase tuning:

$$\begin{aligned}
 \mu(t) &= A \left(\kappa_{FB} \frac{\dot{S}_u[k+1]}{\dot{S}^*} \frac{R^*}{R_u[k+1]} + (1 - \kappa_{FB}) \right) \\
 &\quad (\sin(\omega(t - t_u[k+1]) + \phi^*) - \sin \phi^*) \text{sign}(\bullet)
 \end{aligned} \tag{7.8}$$

where $\text{sign}(\bullet) = 1$ for the left arm and -1 for the right one. The steady-state phase ϕ^* is given by (6.58), with $m = 1$. At time $t = t_u[k+1]$, we obtain the desired impact position ($\mu(t_u[k+1]) = 0$) and the impact velocity:

$$\dot{\mu}(t_u[k+1]) = \kappa_{FB}\dot{\mu}_u[k+1] + (1 - \kappa_{FB})\dot{\mu}^*. \tag{7.9}$$

The amplitude A is tuned to match, in steady-state, the local impact acceleration $\ddot{S}(t_u[k+1])$ with the optimal value defined by (4.21). This acceleration is equal to $\ddot{\mu}(t)$, with μ defined in (7.8), and is obviously negative in steady-state since $0^\circ < \phi^* < 90^\circ$ (see (6.58)).

The feedback gain $0 \leq \kappa_{FB} \leq 1$ is tuned to achieve the best possible trade-off between the stabilizing performance of the observer-based output feedback controller ($\kappa_{FB} = 1$) and its sensitivity to the model uncertainty.

7.3.3 Results

The experimental challenge was to stabilize period-one and, more importantly, period-two orbits of Wiper. This section describes the results we obtained for an aperture of $\theta = 40^\circ$. The parameters of the actuation law (7.8) were tuned to $A = 9^\circ$ and $\omega = 1.1\pi\text{rad/s}$, while the feedback gain has been empirically tuned to $\kappa_{FB} = 0.4$. The coefficient of restitution was estimated about $e = 0.7^3$. The

³The puck used in that experiment was then more elastic than the puck used in the experiments reported in Chapter 6.

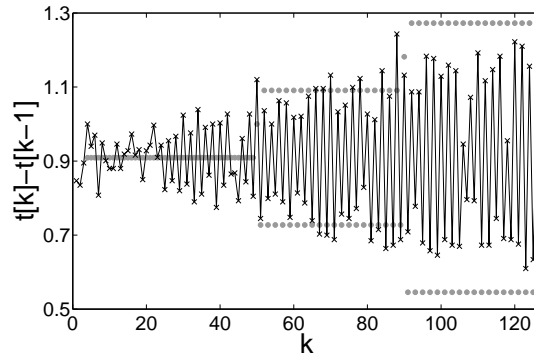


Figure 7.1: The flight times between two successive impacts (detected by the accelerometers) are depicted with the black crosses. The gray circles denote the reference flight times, as defined by $t_\rho[k] - t_\rho[k-1]$. The first part of the trajectory (about $0 < k < 50$) displays the closed-loop stabilization of a period-one motion: $\Delta t^* = \pi/\omega \simeq 0.91$ s. The second part of the trajectory (about $50 < k < 90$) displays the closed-loop stabilization of a “small” period-two motion, i.e. when the reference flight time alternates between $0.9\Delta t^*$ and $1.1\Delta t^*$. The last part of the trajectory (about $k > 90$) displays the closed-loop stabilization of a larger period-two motion: the flight time reference alternates between $0.8\Delta t^*$ and $1.2\Delta t^*$.

experiment initialization has been realized by proper throwing of the puck while the edges were sinusoidally actuated. Initialization then exploited the good basin of attraction of the period-one orbit in open-loop (see Chapter 6). Closed-loop control was switched on after convergence of the observer. Then the reference was switched from period-one to a period-two with small aperture, and finally to a period-two with large aperture. A movie is available⁴ to illustrate this experiment.

The flight times between two successive impacts, as detected by the accelerometers, are depicted in Figure 7.1, w.r.t. the reference. The first part of the trajectory (till $k \simeq 50$) displays the closed-loop stabilization of the period-one motion, i.e. when the target flight time is always equal to $\Delta t^* = \pi/\omega \simeq 0.91$ s. The second part of the trajectory (about $50 < k < 90$) displays the closed-loop stabilization of a “small” period-two motion, i.e. when the flight time alternates between $0.9\Delta t^*$ and $1.1\Delta t^*$. The last part of the trajectory (about $k > 90$) displays the closed-loop stabilization of a larger period-two motion: the flight time reference alternates between $0.8\Delta t^*$ and $1.2\Delta t^*$. The mismatch between the reference and the actual trajectory increases for the “large” period-two orbit. This can be explained as follows: the steady-state velocity \dot{S}^* and impact position R^* depend on the reference pattern (see (6.35), (6.48), (6.49) and (6.51)). However, for the sake of simplicity, we let them equal to the steady-state values of the period-one motion ((6.55) and (6.57))

⁴<http://ieeexplore.ieee.org> (Ronsse et al., 2007a) or on the first author’s homepage. The material is 15.9 MB in size.

in the control law (7.8), regardless of the reference. This introduces a steady-state error w.r.t. the two reference flight times when they significantly differ from each other, when $\alpha \neq 1$.

7.4 Conclusion

The successful experimental validation of period-two orbits in Wiper, with robust control of the trajectory, contrasts with previous results obtained with a sensorless control (Chapter 6 and Ronsse et al., 2006). In that case, indeed, the period-two orbits collapsed after a few seconds. This was due to both the small model-predicted basins of attraction, and the lack of robustness with respect to the real dynamics variability. This illustrates that feedback is required to stabilize the shower pattern with Wiper. A first “naive” attempt to add feedback in Wiper’s dynamics would be to generalize the mirror law algorithms developed by Buehler, Koditschek and Kindlmann (1988, 1990, 1994) for the bouncing ball. However, this law would have sharply contrasted with the encouraging results of the sensorless strategy discussed in Chapter 6, which had already satisfying behavior for the simplest periodic orbit, i.e. the period-one. Indeed, the mirror law requires permanent tracking of the puck in order to measure its continuous-time position and energy (see (3.18)). Such permanent tracking would necessitate a complex sensor design. Preliminary results of the mirror law implementation with a video-based tracker in Wiper can be found in Manuel Gerard’s PhD thesis (Gerard, 2005).

In contrast, we discussed in Chapter 4 an alternative feedback source, based on limited sensing demand: the *impact times*. Indeed, the times of impact can be cheaply measured by accelerometers on the edges (as we did), or microphones, which require limited signal processing to extract the relevant information (see Appendix B.1). This limited sensing led to *robust* control, which compensated for the discrepancies between the model-based observer and the actual dynamics. In agreement with the robustness analysis of Section 4.3, we illustrated that sustained stabilization in the lab required a proper (negative) tuning of the impact acceleration and could never be achieved with positive acceleration.

The present chapter material has been published in Ronsse et al. (2007a).

